Available online at www.sciencedirect.com
ScienceDirect
Comput. Methods Appl. Mech. Engrg. 408 (2023) 115958
Computer methods in applied mechanics and engineering
www.elsevier.com/locate/cma

A novel three-phase mixture approach for the numerical modeling of self-aerated flows

Federico Zabaleta[a,*], Santiago Márquez Damián[b], Fabián A. Bombardelli[a]

[a] Department of Civil and Environmental Engineering, University of California, Davis. 1 Shields Ave, Davis, CA, 95616, USA
[b] Research Center for Computational Methods (CIMEC), Colectora Ruta Nac Nro 168, Km 0, Santa Fe, 3000, Argentina

Received 11 November 2022; received in revised form 16 January 2023; accepted 9 February 2023
Available online xxxx

Abstract

This work presents a novel theoretical/numerical model for the simulation of self-aerated flows under a Reynolds-Averaged Navier-Stokes (RANS) framework. The new formulation is based on a three-phase mixture approach composed of a continuous air phase, a bubble phase, and a continuous water phase. A mass transfer mechanism that does not depend on an entrainment function and does not require calibration accounts for the incorporation of air into the flow. A modification in the formulation of the Volume-of-Fluid algorithm (used to track the free surface) allows one to capture the increase in water depth due to the presence of bubbles. The proposed formulation recovers the traditional Volume-of-Fluid formulation for free surface flows in the absence of bubbles, allowing the model to represent simultaneously the aerated and not aerated regions of a flow. Governing equations for the mixture are derived from mass and momentum conservation equations for each phase, and a numerical algorithm that ensures the boundedness of the numerical solution is proposed. The model is tested and validated using four experimental cases: a degassing tank, a bubble plume, a plunging jet, and a stepped spillway, showing very satisfactory results. The new methodology provides a significant advance in the current capabilities for simulating self-aerated flows.

Keywords: Multiphase flows; Air entrainment; Volume-of-fluid; Two-phase flow

1. Introduction

Air entrainment is the incorporation of pockets of air into the flow due to the strong agitation of the free surface. It occurs in natural flows such as hydraulic jumps, steep mountain rivers, breaking waves, and waterfalls, as well as in man-made structures such as smooth and stepped chutes. The incorporation of air into the flow contributes to restoring dissolved oxygen to water, in addition to diffusive mechanisms. Air entrainment can cause a negative impact if it leads to supersaturation, as it may provoke gas bubble disease in fish [1]. In hydraulic structures, air entrainment plays a fundamental role in the design and during the useful life of the structures. In open channels, high concentrations of air increase the water depth in a process known as bulking, which has to be taken into account when designing sidewalls [2]. The presence of air changes the turbulent flow structures and reduces the wall shear stress, accelerating the flow [3]. Air bubbles also reduce the effect of relative negative pressures, and the risk of cavitation [4].

* Corresponding author.
E-mail address: fzabaleta@ucdavis.edu (F. Zabaleta).

https://doi.org/10.1016/j.cma.2023.115958

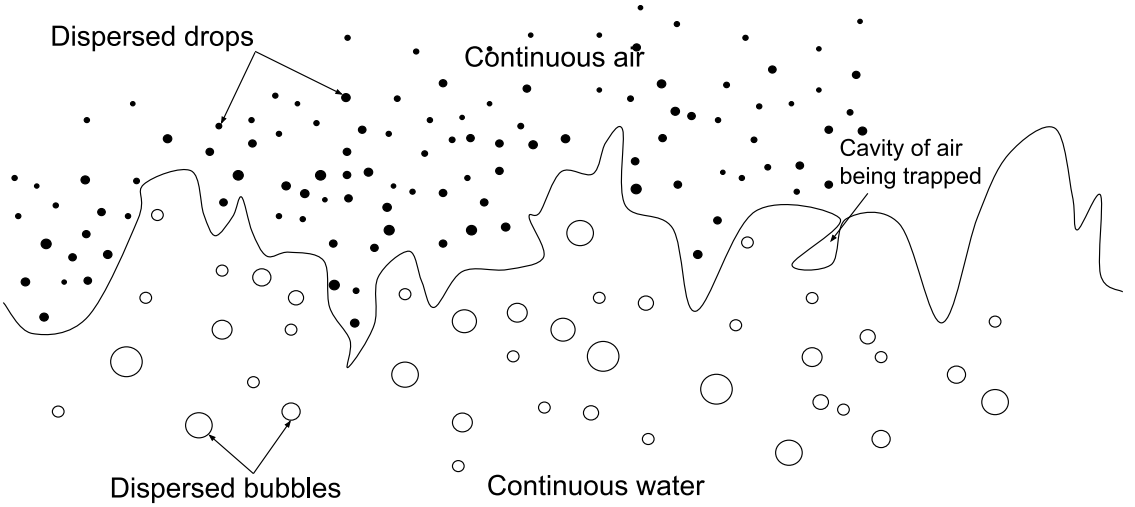

Fig. 1. Scheme of a self-aerated flow (inspired by [7]).

From a fluid mechanics perspective, aeration in free surface flows results from a complex interaction between buoyancy forces, surface-tension forces, and highly turbulent eddies. The gas-liquid interface experiences big distortions that lead to the incorporation of pockets of air into the flow, and to ejections of fluid parcels that are separated from the main flow [5,6]. The air pockets experience break-up and coalescence processes, forming bubbles that are transported along the flow direction and normal to the free surface. The ejections lead to the formation of sprays above the free surface. In Fig. 1, we present a schematic of these phenomena (inspired by [7]). The scales involved in these types of flows range, in the case of open channels, from meters for the water depth and channel width, up to fractions of millimeters for bubbles and droplets.

Self-aerated flows were studied experimentally by Straub and Anderson for rough steep channels [8,9]. They collected an extensive dataset of air distribution for several channel slopes and flow rates. Wood [3] reanalyzed the data of Straub and Anderson, and concluded that the mean air concentration was a function of the channel slope. More recent experimental studies have contributed to the understanding of air-water flows in stepped spillways [10,11], hydraulic jumps [12,13], and plunging jets [14], using conductivity probes [12,14,15], optical probes [13] and image analysis techniques [11]. Experimental methods are often regarded as the most reliable techniques for the prediction of self-aerated flows, but they still present several limitations [16]. Physical modeling of aerated flows is severely affected by scale effects, and very large models are sometimes necessary to predict the aeration in prototype scale. Traditional measuring devices (Acoustic Doppler Velocimetry, Laser Doppler Velocimetry, Particle Image Velocimetry) also have limitations for highly aerated flows, making it challenging to measure velocity profiles and turbulence statistics.

Numerical modeling of self-aerated flows has also proven to be a great challenge. Carrica et al. [17] developed a three-dimensional (3D) polydisperse two-fluid model (TFM) to represent the bubble field around a ship. Air bubbles were introduced through an entrance boundary condition. Other attempts to simulate air entrainment were based upon a sub-grid air-entrainment function that accounts for the incorporation of air through the air-water interface; a transport equation for the bubble phase is then solved inside the water domain. Souders and Hirt [18] pioneered this type of simulations by developing the first air entrainment function for Reynolds-Averaged Navier-Stokes (RANS) simulations. The algorithm represents the incorporation of bubbles at the free surface by performing a comparison between destabilizing and stabilizing forces. When the former are greater than the latter, bubbles are incorporated into the flow. This was first used by Gonzalez and Bombardelli [19] to simulate hydraulic jumps. A similar approach was used by Ma et al. [20], who proposed an air-entrainment model based on the turbulent kinetic energy (TKE) and the gradient of velocities normal to the free surface. The bubbles are entrained using a volumetric source term in an exchange layer located next to the free surface, and transported using a one-way coupled, mono-dispersed model. Castro et al. [21] proposed an air-entrainment model where the bubbles are introduced in the flow by the effect of vortices located near the free surface; they approximated the total entrainment as a linear superposition of

the contribution of each vortex. Lopes et al. [22,23] implemented the model proposed by Ma et al. in the interFoam solver [24], and tested the effect of the mesh resolution for a 2D dam break, and a 3D plunging jet. This model was coupled with an advection-diffusion equation (ADE) to represent the distribution of bubbles in a stepped spillway, obtaining satisfactory results. Dong et al. [25] utilized the model developed by Souder and Hirt embedded in the commercial software *FLOW-3D*® to simulate air entrainment in a stepped spillway. Hohermuth et al. [26] utilized the same software to replicate the experiments of Straub and Anderson [9]. The main advantages of these types of approaches are that they are relatively simple, and the computational cost is significantly lower than any other interface-tracking method for individual bubbles. For these reasons, they have become very popular in engineering applications. On the other hand, the lack of complete understanding of the mechanisms governing the incorporation of air leads to entrainment functions that have to be calibrated for each individual case. For example, the model developed by Ma et al. [20] requires a calibration parameter six times higher for a hydraulic jump than for a plunging jet. In addition, the lack of coupling between the bubble transport model and the interface capturing method for the free surface, does not allow the model to represent the effect of bulking. In some situations, the bulked depth can be five times higher than the equivalent water depth [9], and, therefore, neglecting this effect can have a big impact on the quality of the solution. The only exception to this is the model proposed by Almeland et al. [27], who modified the software developed by Lopes et al. [28] by inverting the direction of the compression velocity in the Volume of Fluid (VOF) method when air is entrained. However, there is not a clear understanding of how this modification is related to the bubble transport equation and the source term in their model. Lopes et al. [28] also showed a figure in which bulking was represented, but the details of how this was achieved are not clear, because their numerical model uses the traditional formulation of VOF and represents the bubble phase as a passive scalar that only modifies the mixture density.

Some studies using Direct Numerical Simulations (DNS) were able to model every turbulent scale and each bubble individually for small domains and low Reynolds numbers [29–32], but this type of approach is unfeasible for most practical applications [21]. A technique that has been gaining popularity in the last few years consists in using the interface-capturing/tracking algorithm to track only the largest pockets of air. Witt et al. [33] simulated a hydraulic jump using a RANS model combined with a VOF technique to represent the free surface and the bubbles entrained in the jump. They showed that, with a very fine mesh, the mean concentration of air inside the jump was similar to the one obtained in the experiments. It is difficult to ascertain the nature of air entrainment in the simulations, considering that RANS models tend to damp most of the free surface fluctuations. Different codes using similar techniques did not incorporate air into the flow [19]. Jesudhas et al. [34] simulated a hydraulic jump using an Improved Delayed Detached Eddy Simulation (IDDES) closure, and were able to reproduce the shape of the air-concentration distributions but not its values. Zabaleta and Bombardelli [6] represented air entrainment in a stepped spillway using a IDDES closure and VOF, but no comparison with measured values of air concentration were performed. Pereira et al. [35] utilized Detached Eddy Simulation (DES) to simulate the flow over a stepped spillway, and employed a hybrid approach similar to the one developed by Márquez Damián and Nigro [36] and Shonibare and Wardle [37]. The authors implemented a dynamic switch based on the phase-fraction gradient to simulate the air phase using pure VOF or a TFM. With this approach, interface features that can be described with the available mesh are tracked individually and features smaller than the mesh size are represented with the TFM. This approach presents an important advantage with respect to the air entrainment function: the flow features that trigger the air entrainment are simulated by the solver, and no empirical correlation between flow parameters and the onset of aeration is needed. Although this method has promising features, there is still a lack of understanding of the effect of the unresolved scales.

In several engineering applications, the scale of the domains makes the usage of eddy-resolving techniques unfeasible. RANS simulations are still (and will be for many years) the method utilized for designing most hydraulic structures and studying river dynamics. Numerical methods to represent self-aerated flows accurately in a RANS framework are highly desirable. In this study, a new framework for the RANS simulation of free surface flows with air entrainment is presented. This framework couples the interface resolving method with the air-entrainment model such that bulking can be represented. Additionally, the traditional idea of an air-entrainment function is discarded and a new method that does not require calibration is proposed. The method is also aimed at contributing with a deeper understanding of the dynamics of air entrainment.

The paper is structured as follows: The conceptual model proposed in this study is described in Section 2. The governing equations for a free surface flow with air entrainment are derived from the Eulerian-Eulerian multiphase

model in Section 3. The numerical methods utilized to solve the governing equations are presented and described in Section 4. In Section 5, the model is validated for four different cases of ascending complexity. In Section 6, the advantages and limitations of the newly proposed method are discussed, the remarks of this study are summarized, and future work is presented.

2. Conceptual model

Self-aerated flows are composed of water and air, whose presence in diverse positions of the flow can be classified as continuous water, continuous air, droplets, and bubbles (see Fig. 1). From a multiphase perspective, self-aerated flows cannot be classified as either dispersed or segregated. Far below the free surface, the flow can be described as a dispersed flow composed of a continuous phase (water) and a dispersed phase (bubbles). Similarly, far above the free surface, the flow can be categorized as a dispersed regime composed of continuous air and water droplets. In the region surrounding the free surface, the flow is not so easily defined. In this region, there is a highly distorted interface that separates continuous water and continuous air, and a great number of bubbles and droplets around it (characterized by Felder and Chanson [38]). Furthermore, the definition of an interface between air and water from a time-averaged perspective is very challenging due to the rapid variation of its position in space and time.

The modeling framework for self-aerated flows is not easy to define because the techniques developed over the years for multiphase flows were either designed for purely dispersed or for purely segregated flows. For dispersed flows, classical techniques include the Lagrangian-Eulerian methods, where each individual particle is followed throughout the fluid, and Eulerian-Eulerian methods, such as the TFM. For segregated flows, interface tracking or interface capturing methods such as VOF, level-set, or Marker-and-Cell (MAC) methods can be used [39]. The methodology used to simulate self-aerated flows has to be able to represent a multiphase flow that transitions from one dispersed regime into another (bubbly water into water spray), through a region that cannot be classified as dispersed or segregated. We would like to note that, under a RANS framework, the capabilities to represent the highly distorted free surface with the interface capturing algorithm are limited by the turbulent closure. In a RANS framework, small-scale turbulent eddies are not represented in the flow field and, therefore, the formation of small-scale features at the interface is limited. Despite the mesh size, while using a RANS model, the free surface in free-surface flows (such as high-speed chutes) will be represented as a mostly smooth surface. In contrast, eddy-resolving closures, such as the one presented in Zabaleta and Bombardelli [6], would allow capturing the small-scale feature at the free surface. We consider important to remark that any proposed model to represent this type of flows will have to be formulated under this intrinsic limitation of the RANS framework.

Following Drew and Passman [40], given a continuous phase indicator χ that is equal to 1 in the water phase and to 0 in the air phase, we define $\langle \chi \rangle = \alpha_W$ as the volume fraction (i.e. mean concentration) of water, and $\langle 1 - \chi \rangle = \alpha_A$ as the volume fraction of air, where the $\langle \cdot \rangle$ operator represents ensemble averaging. In Fig. 2-(a) we show a typical distribution of α_W and α_A for high-velocity, open-channel flows as a function of normalized vertical coordinate z/H_0, where H_0 is the depth at which $\alpha_W = 0$. Near the bottom, $\alpha_W > \alpha_A$, and the flow consists mostly of bubbles in water. Near the top, $\alpha_A > \alpha_W$, and the flow consists mostly of droplets in air. In between these regions, the flow is composed of a mixture of water with bubbles, air with droplets, and a continuous free surface. In the proposed model, we assume that the physics of water-bubble flow dominates when $\alpha_A \leq \alpha_{A,c}$, and that the flow behaves like an air-droplet flow when $\alpha_A > \alpha_{A,c}$. *This means that the flow is represented as an air-droplet flow flowing over a water-bubble flow in a simplified picture of a complex situation*. The transition between these two types of flows is assumed to be sharp. To define the value of $\alpha_{A,c}$, we will use the results of the theoretical study performed by Chanson [7] for open-channel flows. He derived a one-dimensional analytical solution for self-aerated open-channel flows assuming a water-bubbles flow for a concentration of air varying between 0 and 90%. The equation describing this distribution showed good agreement with the air distribution obtained by experiments, indicating that for values of $\alpha_A \leq 0.9$ the flow can be represented as a water-bubble flow. To simplify this model even further, we ignore the dispersed phase in the air-droplet flow and represent it as continuous air flow. Therefore, the droplet phase will not be modeled, and three different phases will be represented: water, air, and bubbles, defined with the phase-fractions α_w, α_a and α_b, respectively. In Fig. 2-(b) we describe how the same distribution of water and air presented in Fig. 2-(a) transforms when using the proposed model. For $z < z_{A,c}$, the flow is composed only of water and bubbles. The phase fraction of bubbles (α_b) varies from 0 at the bottom of the channel up to $\alpha_{A,c}$ at $z_{A,c}$, while the phase fraction of water is calculated as $\alpha_w = 1 - \alpha_b$. Above $z_{A,c}$, $\alpha_{w,b} = 0$ and $\alpha_a = 1$. We would like to highlight that for high air concentrations (α_A), a considerable percentage of this air corresponds to

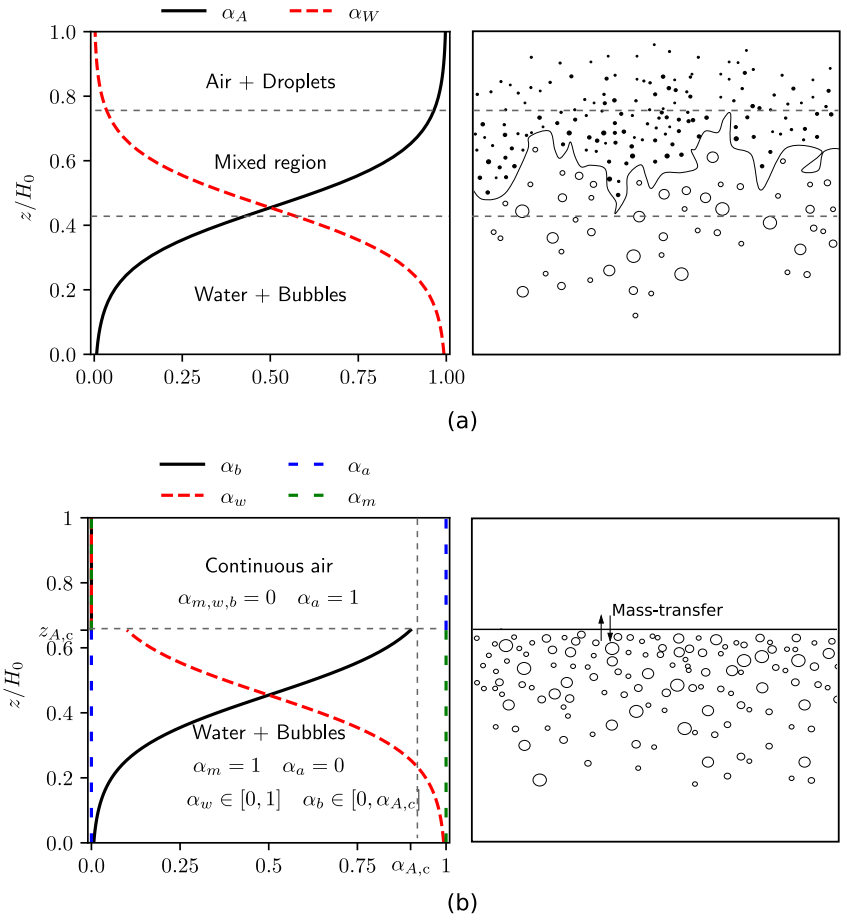

Fig. 2. Mean distribution of air and water and multiphase regime. Real (a) and proposed model (b).

"entrapped" air as opposed to bubbles [41]. The entrapped air (mixed region) is considered in this framework, but it is modeled as dispersed air (following the experience of previous authors). Alternative formulations based on a smooth transition from the water-bubble mixture into the air-droplet mixture could be included in this framework (see Section 3.5). However, the current formulation has been able to provide accurate results in a wide range of applications, as shown in Section 5. These formulations are not studied in this article and are left for future work.

The height at which $\alpha_b = \alpha_{A,c}$ will vary over the domain, and for an open-channel flow, it will depend on the flow rate, the velocity of the flow, and the amount of air incorporated. To calculate the position of the interface between the water-bubble mixture and the continuous air flow, we need to introduce a new variable. We define the water-bubble mixture phase fraction as the sum of the water volume fraction and the bubble phase fraction ($\alpha_m \equiv \alpha_w + \alpha_b$). The water-bubble mixture phase fraction is equal to 1 inside the water-bubble region and equal to 0 in the continuous air region. The distribution of α_m for an open-channel flow is also presented in Fig. 2-(b), which shows that $\alpha_m = 1$ for $z \leq z_{A,c}$ and $\alpha_m = 0$ (i.e. $\alpha_a = 1$) above this point. The definition of this new variable allows for calculating the sharp transition between the water-bubble flow and the continuous air flow using techniques for segregated two-phase flows like the VOF method. Once the position of this interface is calculated, the distribution of bubbles and water within the water-bubble mixture can be obtained using conservation equations for these phases.

To complete this model, it is necessary to represent the incorporation of dispersed air into the flow. During an air-entrainment process, air from the continuous air phase (α_a) is transferred to the bubble phase (α_b). The mechanisms that lead to the incorporation of bubbles (collapsing surface waves for high-speed chutes [42] or instabilities at the impingement region for plunging jets) are represented in the proposed model through a flux of

air from the continuous air phase into the bubble phase. The increment in α_b will lead to an equivalent increment in α_m, which will then move the position of the interface between water-bubble mixture and continuous air. An equivalent, opposite mechanism will occur during a degassing process where bubbles leave the water-bubble mixture and are incorporated into the continuous air phase. This approach leads to a key advantage in the simulation of self-aerated flows: the volume occupied by the water-bubble mixture accounts for the amount of bubbles present in the mixture, and it increases when bubbles are incorporated into the flow and decreases when they leave it. The proposed model provides, to the best of the authors' knowledge, for the first time, a framework in which bulking can be represented under a full 3D RANS simulation. Another advantage of the current formulation is that when no bubbles are entrained and the water-bubble mixture is only composed of water (i.e., $\alpha_m = \alpha_w$), the model can be used to represent purely segregated flows. This is very useful because most self-aerated flows only present air entrainment in a constrained region. For example, in plunging jets, air entrainment occurs only on a small region surrounding the jet, but, far from it, the free surface is clearly defined and no bubbles are present under the free surface. Something similar happens on spillways where air is incorporated only after the inception point. Before this point, the flow consists of pure water flowing over the spillway with a clear separation between water and air. The new methodology allows calculating both regions simultaneously with the same model.

The key aspects and most important implications of the proposed model can be detailed as follows:

- Flow is represented as continuous air flowing over a water-bubble mixture.
- Three phases are considered in this formulation: a water phase (α_w), a bubble phase (α_b) and continuous air phase (α_a).
- The interface between the continuous air and the water-bubble mixture is calculated using a transport equation for the water-bubble mixture phase fraction defined as $\alpha_m \equiv \alpha_w + \alpha_b$.
- The incorporation of air into the flow due to surface instabilities is accounted for through a mass-transfer term that transfers mass from the continuous air phase (α_a) into the bubble phase (α_b), and thus into the water-bubble mixture phase (α_m)
- The introduction of the water-bubble mixture as a main variable allows to represent the modification of the free surface location due to the presence of bubbles.
- The current formulation can be used simultaneously for dispersed and segregated flows.
- Alternative formulations for the treatment of the dispersed phase could be easily implemented in this framework. However, the current formulation has been able to provide accurate results in a relatively wide range of applications, as shown in Section 5.

3. Mathematical formulation

Equations are derived starting from conservation laws for the kth phase obtained by ensemble averaging [40,43], as follows:

$$\frac{\partial \alpha_k \rho_k}{\partial t} + \nabla \cdot (\alpha_k \rho_k \mathbf{v}_k) = S_k^*, \tag{1}$$

$$\frac{\partial \alpha_k \rho_k \mathbf{v}_k}{\partial t} + \nabla \cdot (\alpha_k \rho_k \mathbf{v}_k \mathbf{v}_k) = -\nabla \cdot \alpha_k p_k \mathbf{I} + \nabla \cdot \left[\alpha_k \left(\mathbf{T}_k + \mathbf{T}_{\mathbf{t},k}\right)\right] + \alpha_k \rho_k \mathbf{g} + \boldsymbol{m}_k, \tag{2}$$

where k is the phase indicator and $\sum \alpha_k = 1$. Eq. (1) represents the mass conservation of phase k and Eq. (2) indicates the momentum conservation of phase k. In these equations, α_k is the phase volume fraction, ρ_k the density, $\mathbf{v}_k$ the velocity vector, S_k^* the source term, p_k the pressure, $\mathbf{T}_k$ the viscous stress tensor, $\mathbf{T}_{\mathbf{t},k}$ the remaining stresses from the averaging process, $\mathbf{g}$ the acceleration of gravity and $\mathbf{m}_k$ the interaction forces.

The mathematical model proposed in this study is based on the mixture formulation. In a mixture approach, the phase velocities are averaged and replaced by the velocity of the mixture. The mixture velocity is obtained from the momentum conservation equation for the mixture, whereas the distributions of phases are obtained from the mass conservation equations for each phase. The differences in velocity between phases are represented with slip velocities, which are calculated with algebraic models. Depending on how these velocities are calculated, the mixture model can be used to represent segregated or dispersed flows [36]. In the problem at hand, the three phases are $k = a$ (air), $k = b$ (bubbles), and $k = w$ (water). We denote with S_k^* the source term representing the mass transfer between the continuous air phase and the bubble phase. This means that $S_b^* = -S_a^*$ and $S_w^* = 0$. The

governing equations for the mixture are derived using similar methods to the ones proposed by Bohorquez [44], and Ouda and Toorman [45], for sediment transport.

The three-phase mixture equations are defined in terms of mixture density (ρ), mass-weighted mixture velocity ($\mathbf{v}$) and volume-weighted mixture velocity ($\mathbf{u}$), defined as follows:

$$\rho = \sum_k \alpha_k \rho_k; \quad \mathbf{v} = \frac{1}{\rho} \sum_k \alpha_k \rho_k \mathbf{v}_k; \quad \mathbf{u} = \sum_k \alpha_k \mathbf{v}_k. \tag{3}$$

The set of equations are established by using five scalar variables (α_w, α_b, α_a, p and ρ), and one vectorial variable ($\mathbf{v}$ or $\mathbf{u}$). The three volume-phase-fractions add up to one, and the density is related to the phase-fractions by Eq. (3). This means that to solve this system, five equations are needed. In this approach, we solve the mass conservation equations for the water-bubble mixture (α_m) and for the bubble phase (α_b). Additionally, the mass conservation for the three-phase mixture (water-bubble-air) is used to derive the pressure equation. Finally, the momentum conservation equation for the three-phase mixture is used to obtain the mixture velocity ($\mathbf{v}$). The inclusion of the water-bubble mixture as a variable allows us to make a slight modification in the classical definition of the VOF method and couple the bubble transport equation with the method for solving the free surface. Some quantities for this new variable are defined following Eq. (3):

$$\rho_m \equiv \frac{\alpha_w \rho_w + \alpha_b \rho_b}{\alpha_m}; \quad \mathbf{u}_m \equiv \frac{\alpha_w \mathbf{v}_w + \alpha_b \mathbf{v}_b}{\alpha_m}; \quad \mathbf{v}_m \equiv \frac{\rho_w \alpha_w \mathbf{v}_w + \rho_b \alpha_b \mathbf{v}_b}{\rho_m \alpha_m} \tag{4}$$

In addition to the variables mentioned above, two relative velocities between the phases are introduced, for which algebraic models are provided. The relative velocities between the water and bubble phase ($\mathbf{v}_{b-w}$) and between the water-bubble mixture and air phase ($\mathbf{u}_{m-a}$), are defined as:

$$\mathbf{v}_{b-w} \equiv \mathbf{v}_b - \mathbf{v}_w; \quad \mathbf{u}_{m-a} \equiv \mathbf{u}_m - \mathbf{v}_a \tag{5}$$

In the following sections, for the sake of brevity, the three-phase mixture will be simply referred as “mixture”, while the water-bubble mixture will still be named by its full name.

3.1. Mass conservation for the mixture

The mass conservation equation for the mixture in terms of the volume-weighted mixture velocity can be obtained by taking ρ_k common factor from Eq. (1), summing over k and applying previous definitions. The resulting equation is:

$$\nabla \cdot \mathbf{u} = 0, \tag{6}$$

showing that the volume-weighted velocity is divergence-free. This equation is used to derive the pressure equation. It can be shown that (Supplementary Material, Appendix A, Identity 1) the volume weighted velocity ($\mathbf{u}$) and the mass-weighted velocity ($\mathbf{v}$) are related by

$$\mathbf{u} = \mathbf{v} - \alpha_m(1-\alpha_m)\frac{\rho_m - \rho_a}{\rho}\mathbf{u}_{m-a} - \alpha_b s \frac{\alpha_w}{\alpha_m + \alpha_b s}\frac{\rho_m}{\rho}\mathbf{v}_{b-w}, \tag{7}$$

where $s = \rho_b/\rho_w - 1$ and, therefore, the mass conservation equation for the mixture can be written as:

$$\nabla \cdot \mathbf{v} = \nabla \cdot \left[\alpha_m(1-\alpha_m)\frac{\rho_m - \rho_a}{\rho}\mathbf{u}_{m-a} + \alpha_b s \frac{\alpha_w}{\alpha_m + \alpha_b s}\frac{\rho_m}{\rho}\mathbf{v}_{b-w} \right] \tag{8}$$

3.2. Mass conservation for the water-bubble mixture

The conservation equation for the water-bubble mixture is obtained by taking common factor ρ_k of Eq. (1), and adding for $k = \{w, b\}$:

$$\frac{\partial \alpha_m}{\partial t} + \nabla \cdot (\alpha_m \mathbf{u}_m) = S_b. \tag{9}$$

where $S_b = S_b^*/\rho_b$ is the volume transfer term. $\mathbf{u}_m$ is not selected as one of the main variables in this model, so it has to be expressed in terms of the mixture velocity ($\mathbf{u}$) and relative velocities. It can be shown (Supplementary Material, Appendix A, Identity 3) that

$$\mathbf{u}_m = \mathbf{u} + (1 - \alpha_m)\mathbf{u}_{m-a}. \tag{10}$$

Substituting (10) in (9), the conservation equation for the water-bubble mixture in terms of mixture velocity is obtained:

$$\frac{\partial \alpha_m}{\partial t} + \nabla \cdot (\alpha_m \mathbf{u}) + \nabla \cdot [\alpha_m(1 - \alpha_m)\mathbf{u}_{m-a}] = S_b. \tag{11}$$

Note that this equation resembles the equation used in the VOF algorithm, with the exception of the source term.

3.3. Mass conservation for the bubble phase

The bubble velocity ($\mathbf{v}_b$) can be expressed in terms of mixture velocity and relative velocities (Supplementary Material, Appendix A, Identity 4) as:

$$\mathbf{v}_b = \mathbf{u} + (1 - \alpha_m)\mathbf{u}_{m-a} + \frac{\alpha_w}{\alpha_m}\mathbf{v}_{b-w} \tag{12}$$

Substituting (12) in (1), for $k = b$, the mass conservation equation for the bubble phase in terms of the main variables is obtained:

$$\frac{\partial \alpha_b}{\partial t} + \nabla \cdot (\alpha_b \mathbf{u}) + \nabla \cdot \left[\alpha_b \left((1 - \alpha_m)\mathbf{u}_{m-a} + \frac{\alpha_w}{\alpha_m}\mathbf{v}_{b-w}\right)\right] = S_b \tag{13}$$

3.4. Momentum conservation for the mixture

The momentum equation for the mixture is obtained by summing the momentum equations over the three phases. For the sum of temporal derivatives, the definition of mass-weighted velocity can be applied directly:

$$\sum_k \frac{\partial \alpha_k \rho_k \mathbf{v}_k}{\partial t} = \frac{\partial \rho \mathbf{v}}{\partial t}. \tag{14}$$

Using the customary assumption that pressures corresponding to all phases are in microscopic equilibrium (i.e., $p_k = p$) [46], the pressure term is simplified as:

$$-\sum_k \nabla(\alpha_k p_k) = -\nabla p. \tag{15}$$

The gravitational acceleration term gives:

$$\sum_k \alpha_k \rho_k \mathbf{g} = \rho \mathbf{g} \tag{16}$$

If we define the reduced pressure as $p_{rgh} \equiv p - \rho \mathbf{g} \cdot \mathbf{x}$, where $\mathbf{x}$ is the position vector, we can rewrite the pressure and gravity terms as:

$$-\nabla p + \rho \mathbf{g} = -\nabla p_{rgh} - \mathbf{g} \cdot \mathbf{x} \nabla \rho, \tag{17}$$

which provides several advantages in terms of stability and in the definition of the boundary conditions [47]. For the viscous and turbulent stress tensors, the generalized shear stress approach [48] is utilized, resulting in the following:

$$\sum_k \left[\alpha_k \left(\mathbf{T}_k + \mathbf{T}_{\mathbf{t},k}\right)\right] = \mu_{\text{eff}} \left(\nabla \mathbf{v} + \nabla \mathbf{v}^T\right), \tag{18}$$

where $\mu_{\text{eff}} = \mu + \mu_T$ is the sum of the viscous and turbulent viscosity of the three-phase mixture, and $\mu = \sum_k \alpha_k \mu_k$. The interaction forces cancel when adding up for the three phases, except for the surface tension force, therefore

$$\sum_k \mathbf{m}_k = \mathbf{f}_\sigma \tag{19}$$

For the sum of the advective terms, it can be shown (Supplementary Material, Appendix A, Identity 5) that:

$$\sum_k \alpha_k \rho_k \mathbf{v}_k \mathbf{v}_k = \rho \mathbf{v}\mathbf{v} + \alpha_b \left(1 - \frac{\alpha_b}{\alpha_m}\right) \frac{\rho_b \rho_w}{\rho_m} \mathbf{v}_{b-w} \mathbf{v}_{b-w} + \alpha_m \alpha_a \frac{\rho_a \rho_m}{\rho} \mathbf{v}_{m-a} \mathbf{v}_{m-a} \tag{20}$$

where

$$\mathbf{v}_{m-a} \equiv \mathbf{v}_m - \mathbf{v}_a = \mathbf{u}_{m-a} + \alpha_b s \frac{\alpha_w}{\alpha_m(\alpha_m + \alpha_b)s} \mathbf{v}_{b-w} \tag{21}$$

These operations result in the momentum conservation equation for the mixture:

$$\frac{\partial \rho \mathbf{v}}{\partial t} + \nabla \cdot (\rho \mathbf{v}\mathbf{v}) = -\nabla p_{rgh} + \nabla \cdot \left(\mu_{\text{eff}} \left(\nabla \mathbf{v} + \nabla \mathbf{v}^T\right) + \mathbf{T}_{b-w} + \mathbf{T}_{m-a}\right) - \mathbf{g} \cdot \mathbf{x} \nabla \rho + \boldsymbol{f}_\sigma \tag{22}$$

where the tensors $\mathbf{T}_{b-w}$ and $\mathbf{T}_{m-a}$ represent the momentum diffusion due to the relative motion between phases and are defined as:

$$\mathbf{T}_{b-w} = -\alpha_b \left(1 - \frac{\alpha_b}{\alpha_m}\right) \frac{\rho_b \rho_w}{\rho_m} \mathbf{v}_{b-w} \mathbf{v}_{b-w} \tag{23}$$

$$\mathbf{T}_{m-a} = -\alpha_m \alpha_a \frac{\rho_a \rho_m}{\rho} \mathbf{v}_{m-a} \mathbf{v}_{m-a} \tag{24}$$

3.5. Relative velocities

The relative velocity between the bubble and water phase ($\mathbf{v}_{b-w}$) is split into a component due to buoyancy and another one due to turbulent fluctuations [49]:

$$\mathbf{v}_{b-w} = \sqrt{\alpha_w} \mathbf{v}_{b-w}^{\infty} + \frac{D_b}{\alpha_b} \nabla \alpha_b, \tag{25}$$

where $\mathbf{v}_{b-w}^{\infty}$ is the terminal slip velocity of a single bubble, and D_b is the turbulent diffusivity. The first term results from a balance of gravity and drag forces. In the case of bubbles, this analysis is more complex than for rigid spheres. The shape of the bubble influences the drag and, therefore, the terminal rising velocity. In addition, impurities in the water phase cause important modifications in the terminal velocity. Grace [50] proposed a diagram in which size, shape, and rising velocity of one bubble in an infinite medium can be obtained from the relation among three dimensionless numbers: Eotvos number, Morton number, and Reynolds number. For the sake of simplicity, in this study we have adopted a simple parameterization proposed by Wüest et al. [51]:

$$\mathbf{v}_{b-w}^{\infty} = \begin{cases} -4474 r_b^{1.357} \hat{\mathbf{g}} & \text{if } 0 < r_b \leq 7 \times 10^{-4} \\ -0.23 \hat{\mathbf{g}} & \text{if } 7 \times 10^{-4} < r_b \leq 5.1 \times 10^{-3} \\ -4.202 r_b^{0.547} \hat{\mathbf{g}} & \text{if } r_b > 5.1 \times 10^{-3} \end{cases} \tag{26}$$

where $\hat{\mathbf{g}} = \mathbf{g}/|\mathbf{g}|$. The diffusivity of the bubble is considered proportional to the eddy viscosity, $D_b = \nu_T / Sc$, where Sc is the turbulent Schmidt Number. After substituting Eq. (25) into Eq. (13), the mass conservation equation for the bubble presents the structure of an advection-diffusion equation:

$$\frac{\partial \alpha_b}{\partial t} + \nabla \cdot (\alpha_b \mathbf{u}) + \nabla \cdot \left[\alpha_b \left((1 - \alpha_m)\mathbf{u}_{m-a} + \frac{\alpha_w^{1.5}}{\alpha_m} \mathbf{v}_{b-w}^{\infty}\right)\right] + \nabla \cdot \left(\frac{\alpha_w}{\alpha_m} D_b \nabla \alpha_b\right) = S_b \tag{27}$$

It is worth noting that alternative formulations could be used for $\mathbf{v}_{b-w}$. Expressions based on blending of the ascending velocity of a single bubble, and falling velocity of a water droplet, as a function of the dispersed air phase fraction, could allow the model to be extended to air concentrations higher than 90%.

The relative velocity between the water-bubble mixture and the air phase ($\mathbf{u}_{m-a}$) is an artificial compressive velocity used to avoid numerical diffusion on the interface [52] defined as:

$$\mathbf{u}_{m-a} = C_\alpha |\mathbf{u}| \frac{\nabla \alpha_m}{|\nabla \alpha_m|}, \tag{28}$$

where C_α is a proportionality constant.

3.6. Volume transfer term

The volume transfer term represents the transformation of the continuous air phase into the bubble phase and vice versa. This term accounts for the mechanisms that lead to the incorporation of bubbles that cannot be represented with the interface-capturing algorithm under a RANS framework. When turbulence is strong enough at the free surface such that air can be entrained, continuous air is transformed into bubbles. When conditions in the free surface are calmer, bubbles are transformed into continuous air (detrainment). The volume transfer term is then divided into a source term (incorporation of bubbles, S_b^+) and a sink term (elimination of bubbles, S_b^-):

$$S_b = \phi S_b^+ - (1-\phi) S_b^- \tag{29}$$

where ϕ is a switch indicating where air is entrained (it is equal to 1 when air is entrained and equal to 0 when air leaves the water-bubble mixture). In general, ϕ is a function of flow mean parameters ($\phi = \phi\,(\mathbf{u}, \rho_w, \rho_a, \sigma, k, \epsilon)$). Several authors have attempted to define the occurrence of air entrainment based on mean parameters of the flow [18,53]. In this study, for the sake of simplicity, ϕ is assigned manually based on the experimental data.

Ideally, the transformation of continuous air into bubbles would take place inside the entrapped pockets of air. Under a RANS framework, this type of pockets do not always appear (see, for example, a RANS representation of a high-velocity open-channel flow). For this reason, we assume that the transformation of air into bubbles occurs in a fictitious thin region immediately above the free surface $N_{\mathrm{FS},1}$, defined as $N_{\mathrm{FS},1} = \{\mathbf{x} \in \mathbf{R}^3 : |\mathbf{x} - \mathbf{p}_{FS}| \leq \delta s,\ \alpha_a(\mathbf{x}) > 0\}$, where $\mathbf{p}_{FS}$ is the closest point on the free surface to $\mathbf{x}$, and δs is the thickness of this region. Because the term S_b^+ accounts for the transformation of continuous air into bubbles, it can only take positive values where $\alpha_a > 0$. The calculation of S_b^+ arises from the definition of the model itself. At the interface between α_m and α_a, the concentration of bubbles (α_b) has to be equal to 0.9 when air is entrained. Then the source term is calculated such that α_b in the region near the free surface ($N_{\mathrm{FS},1}$) reaches the value of 0.9 in a short period of time (δt). Then S_b^+ is calculated as:

$$S_b^+ = \frac{0.9}{\delta t} H\,(0.9 - \alpha_b)\,\xi_1 \tag{30}$$

where $H()$ is the Heaviside step function and ξ_1 is an indicator that takes the value of 1 inside $N_{\mathrm{FS},1}$ and 0 away from it. We assume that the rate of transformation from continuous air to bubbles is proportional to the flux of water-bubble mixture, and therefore $\delta t = k_1 \delta s / \mathbf{v}$ where k_1 is a proportionality constant. This formulation leads to the formation of a thin layer of bubbles above the water surface that can be advected or diffused into the flow. It is important to notice that without an advective or diffusive process that carries the bubbles into the water-bubble mixture domain, bubbles would be contained in this thin region and would not generate any entrainment into the flow. Once bubbles are transported from this thin region into the water-bubble mixture, S_b^+ only transforms enough continuous air into bubbles to maintain the concentration at the free surface equal to 0.9. For this reason, S_b^+ does not represent (like in previous attempts to represent air entrainment) an air entrainment function, but only a transformation of continuous air (that cannot be advected and diffused into the flow), into dispersed air (that can be advected and diffused into the flow). In fact, the rate of air entrainment under this formulation is equal to the total flux of bubbles calculated from Eq. (13) as $[\alpha_b \mathbf{u} + \alpha_b \alpha_a \mathbf{u}_{m-a} + \alpha_b(\alpha_w/\alpha_m)\mathbf{v}_{b-w}]_{N_{FS,1}}$. This accounts for the balance between bubble entrainment/detrainment traditionally described in the literature [7,20] without any ad-hoc function (entrainment function).

The sink term is calculated analogously to the source term. When air is detrained ($\phi = 0$), bubbles that reach the free surface are transformed into continuous air. Bubble transformation into continuous air takes place in a small region immediately below the free surface ($N_{\mathrm{FS},2}$), defined as $N_{\mathrm{FS},2} = \{\mathbf{x} \in \mathbf{R}^3 : |\mathbf{x} - \mathbf{p}_{FS}| \leq \delta s,\ \alpha_b(\mathbf{x}) > 0\}$. The rate of transformation from bubble to air is calculated similarly to the rate of transformation of air into bubbles. Then, S_b^- is calculated as:

$$S_b^- = \frac{0.9}{\delta t} H(\alpha_b)\xi_2 \tag{31}$$

where ξ_2 is an indicator that takes the value of 1 inside $N_{\mathrm{FS},2}$ and 0 away from it. In Fig. 3, we present a schematic description of the volume transfer calculation. Overall, this formulation has allowed for a satisfactory representation of the air entrainment (S_b^+) or detrainment (S_b^-).

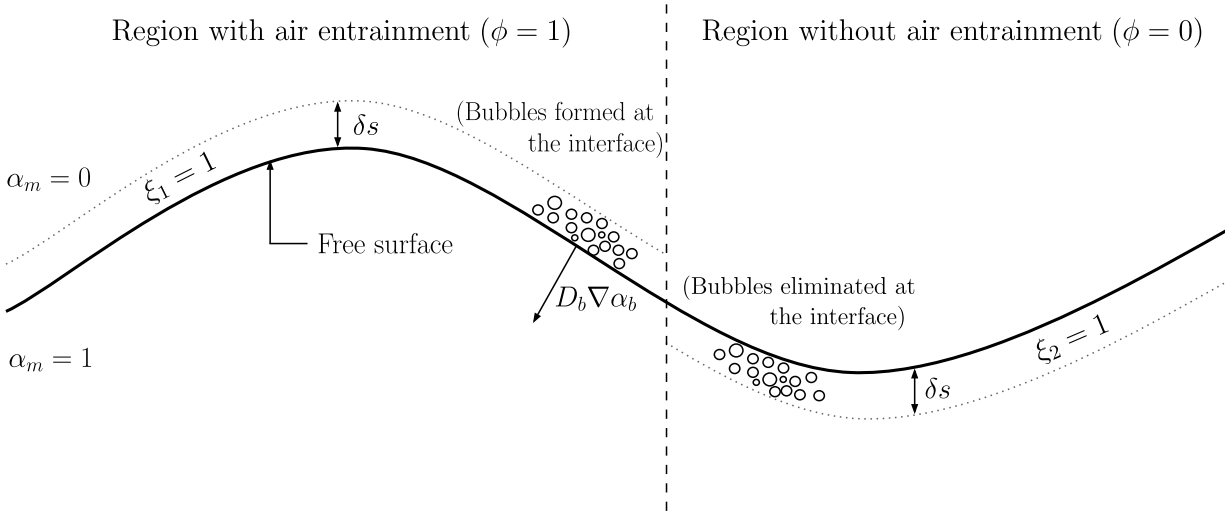

Fig. 3. Schematic description of mass transfer term.

4. Numerical implementation

The numerical implementation of the model is performed using the Finite Volume Method (FVM). The implementation is undertaken by using the OpenFOAM platform [24,54]. The pressure-velocity decoupling is resolved using the PIMPLE algorithm, which is a combination of the PISO and SIMPLE algorithms [55]. In Fig. 4, we present a flow chart describing the structure of the solver. First, the relative velocities are calculated by Eqs. (25) and (28). Then, the new distributions of the water-bubble mixture and bubble phase volume fractions are obtained by solving Eqs. (11) and (13), using a flux-limited solver. After this step, the mixture velocity and pressure are obtained by solving the momentum and pressure equations. Finally, the turbulence model is solved and the mixture density and viscosity are updated. In the following sub-sections, each of these steps is thoroughly described.

4.1. Solution of the water-bubble mixture and bubble conservation equations

The semi-discretized version [56] of Eqs. (11) and (27) can be written by using the divergence theorem respectively as:

$$\frac{\partial \alpha_m}{\partial t} V_C + \sum_f F_u \alpha_{m,f} + \sum_f (1 - \alpha_{m,f}) F_{m-a} \alpha_{m,f} = S_b V_C \tag{32}$$

$$\frac{\partial \alpha_b}{\partial t} V_C + \sum_f F_u \alpha_{b,f} + \sum_f \left[(1 - \alpha_{m,f}) F_{m-a} + \frac{\alpha_{w,f}^{1.5}}{\alpha_{m,f}} F_{b-w} \right] \alpha_{b,f} + \sum_f \frac{\alpha_{w,f}}{\alpha_{m,f}} D_{b,f} \nabla \alpha_{b,f} = S_b V_C \tag{33}$$

where the sub-index f refers to quantities evaluated at the cell face, V_C is the cell's volume, and F_u, F_{m-a} and F_{b-w} are velocity face fluxes defined as:

$$F_u = \mathbf{u} \cdot \mathbf{S}_f, \quad F_{m-a} = \mathbf{u}_{m-a} \cdot \mathbf{S}_f, \quad F_{b-w} = \mathbf{v}_{b-w}^{\infty} \cdot \mathbf{S}_f, \tag{34}$$

where $\mathbf{S}_f$ the face normal vector.

The numerical method employed to solve this system of equations has to guarantee three properties:

1. The solution should be bounded between 0 and 1 ($0 \leq (\alpha_m, \alpha_b) \leq 1$).
2. The solution cannot create new local maxima or minima ($\alpha_m^{\text{minG}} \leq \alpha_m \leq \alpha_m^{\text{maxG}}$).
3. The value of α_m have to be greater or equal than α_b everywhere in the domain ($\alpha_m \geq \alpha_b$).

A technique that guarantees the first two properties is the Multidimensional Universal Limiter for Explicit Solution (MULES). MULES is the OpenFOAM implementation of the Flux Corrected Transport (FCT) method [57], which

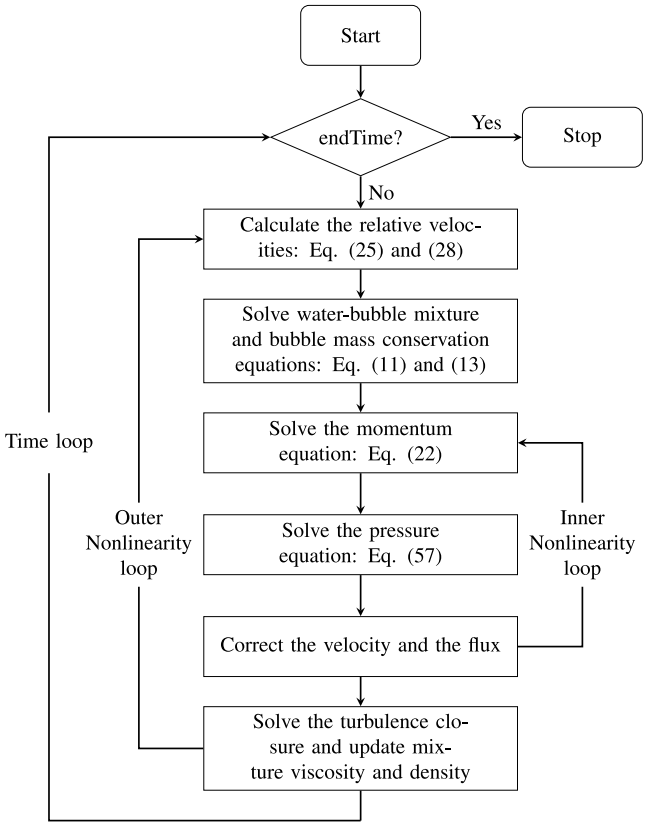

Fig. 4. Flow-chart describing the structure of the air entrainment solver.

is designed to ensure boundness in the solution of hyperbolic problems by limiting the fluxes at the cell faces. MULES, however, was not intended to guarantee the third property, and several tests performed by the authors corroborated such fact. In this study, we implement some modifications into the MULES algorithm to enforce the third property as well. For details on the original MULES algorithm, the reader is referred to the work of Márquez Damián [58], but we offer some information herein.

Using an explicit forward Euler discretization for the time derivative, Eq. (32) can be manipulated to obtain the value of the water-bubble mixture phase fraction at the new time step ($\alpha_m^{t+\Delta t}$):

$$\alpha_m^{t+\Delta t} = \alpha_m^t - \frac{\Delta t}{V_C}\sum_f F_m^t + \Delta t S_b \tag{35}$$

where Δt is the time step and F_m is the total water-bubble mixture flux defined as:

$$F_m = \alpha_{m,f}\left[F_{\mathbf{u}} - (1-\alpha_{m,f})F_{m-a}\right] \tag{36}$$

From this expression, it can be noticed that the value of $\alpha_m^{t+\Delta t}$ can be bounded by limiting the value of F_m. This flux can be divided into a low-order flux (F_m^L) which guarantees a monotonic and bounded solution [59], and a correction or anti-diffusive flux (F_m^C):

$$F_m^L = F_u\alpha_{m,f}^L; \quad F_m^C = \alpha_{m,f}^H\left[F_{\mathbf{u}} - (1-\alpha_{m,f})F_{m-a}\right] - F_m^L, \tag{37}$$

where the superscripts L and H represent low-order and high-order interpolation values, respectively. The inclusion of the correction flux can introduce unboundedness to the solution. To avoid this, the flux is limited using a coefficient λ which takes values between 0 and 1. Then the limited flux is defined as $F_m^{\lim} = F_m^U + \lambda_m F_m^C$.

Using an explicit scheme (such as MULES) for Eq. (33) would require excessively small time steps due to the presence of a stiff term (diffusion), and an implicit scheme would not guarantee the three properties mentioned

above. For these reasons, an implicit-explicit method [60] is used to solve the bubble transport equation: the advective terms are solved using an explicit scheme, and an implicit scheme is used for the diffusive terms. Eq. (33) is divided into two sets of equations as follows:

$$\frac{\alpha_b' - \alpha_b^t}{\Delta t} V_C + \sum_f \left[F_u \alpha_{b,f}\right]^t + \sum_f \left[(1-\alpha_{m,f})F_{m-a}\alpha_{b,f} + \frac{\alpha_{w,f}^{1.5}}{\alpha_{m,f}} F_{b-w}\alpha_{b,f}\right]^t = S_b^t V_C \tag{38}$$

$$\frac{\alpha_b^{t+\Delta t} - \alpha_b'}{\Delta t} V_C + \sum_f \left[\frac{\alpha_{w,f}}{\alpha_{m,f}} D_{b,f} \nabla \alpha_{b,f}\right]^{t+\Delta t} = 0 \tag{39}$$

Eq. (38) can be solved using a similar technique as explained above, while Eq. (39) can be solved using an implicit scheme. In order to guarantee that $\alpha_b \leq \alpha_m$ after solving the diffusion equation, the bubble diffusivity has to be limited adequately. This is done by limiting $D_{b,f}$ on the faces such that α_b can only be diffused to cells with water-bubble mixture volume-phase-fraction (α_m) close to 1.

A similar procedure can be adopted for Eq. (38):

$$\alpha_b' = \alpha_b^t - \frac{\Delta t}{V_C} \sum_f F_b^t + \Delta t S_b = \alpha_b^t - \frac{\Delta t}{V_C} \sum_f (F_b^{L,t} + F_b^{C,t}) + \Delta t S_b \tag{40}$$

where

$$F_b = \alpha_{b,f} \left[F_{\mathbf{u}} - (1-\alpha_{m,f})F_{m-a} + \frac{\alpha_{w,f}^{1.5}}{\alpha_{m,f}} F_{b-w}\right] \tag{41}$$

$$F_b^L = F_u \alpha_{b,f}^L; \quad F_b^C = \alpha_{b,f}^H \left[F_{\mathbf{u}} - (1-\alpha_{m,f})F_{m-a} + \frac{\alpha_{w,f}^{1.5}}{\alpha_{m,f}} F_{b-w}\right] - F_b^L, \tag{42}$$

and then the limited value of the total bubble flux defined as $F_b^{\lim} = F_b^U + \lambda_b F_b^C$. Due to the presence of additional limiters in the calculation of S_b (see Section 4.3), the calculation of $\alpha_m^{t+\Delta t}$ and $\alpha_b^{t+\Delta t}$ is performed in three steps. First, the source term is added:

$$\alpha_m^* = \alpha_m^t + \Delta t S_b \tag{43}$$

$$\alpha_b^* = \alpha_b^t + \Delta t S_b \tag{44}$$

The source term is added individually because S_b is limited by the amount of continuous air on the cell, and performing this calculation with the summation of the fluxes at the same time could lead to negative values of a phase-fraction. It follows that if $\alpha_m^t \geq \alpha_b^t$, then $\alpha_m^* \geq \alpha_b^*$. On a second step, the low-order fluxes are added:

$$\alpha_m^{**} = \alpha_m^* + \frac{\Delta t}{V_C} \sum_f F_m^{L,t} \tag{45}$$

$$\alpha_b^{**} = \alpha_b^* + \frac{\Delta t}{V_C} \sum_f F_b^{L,t} \tag{46}$$

By adding the low-order fluxes, α_m^{**} and α_b^{**} remain bounded and no local maxima or minima are created. It can also be shown that if $\alpha_m^* \geq \alpha_b^*$, and the Courant Number is smaller or equal than 1 (CN $\leq$ 1), then $\alpha_m^{**} \geq \alpha_b^{**}$ (see Supplementary Material, Appendix B). Finally, the limited correction fluxes are added:

$$\alpha_m^{t+\Delta t} = \alpha_m^{**} + \frac{\Delta t}{V_C} \sum_f \lambda_m F_m^{C,t} \tag{47}$$

$$\alpha_b' = \alpha_b^{**} + \frac{\Delta t}{V_C} \sum_f \lambda_b F_b^{C,t} \tag{48}$$

The values of λ_m and λ_b are calculated using the traditional formulation of Zalesak [57]. Even though this formulation is more diffusive than the iterative method implemented in the MULES algorithm [58], it guarantees strict boundedness under all circumstances. The solver developed in this work is sensitive to negative values of α_w (which appear when $\alpha_b > \alpha_m$), leading rapidly to negative values of density, and making the solver unstable.

The minimum value of α_m is defined as $\alpha_m^{\min} = \min\left[0, \alpha_b^{**}, \alpha_m^{\min G}\right]$ and the maximum value of α_b is defined as $\alpha_b^{\max} = \max\left[1, \alpha_m^{t+\Delta t}\right]$. During the solution of these equations, the relative velocity fluxes (F_{m-a} and F_{b-w}) are limited because they form part of the correction fluxes. Therefore, their limited values ($F_{m-a}^{\lim} = \lambda_m \lambda_b F_{m-a}$ and $F_{b-w}^{\lim} = \lambda_b F_{b-w}$) are used in the resolution of the momentum and pressure equations.

4.2. Solution of the momentum and pressure equations

Eq. (22) is written in its semi-discretized version as:

$$\frac{\partial \rho \mathbf{v}}{\partial t} V_C + \sum_k (F_{\rho \mathbf{v}}) \mathbf{v}_f - \sum_k \mu_{tot} \nabla \mathbf{v}_f \cdot \mathbf{S}_f = \sum_k \left(\mathbf{T}_{b-w,f} + \mathbf{T}_{\gamma-a,f}\right) \cdot \mathbf{S}_f - \nabla p_{rgh} - \mathbf{g} \cdot \mathbf{x} \nabla \rho + \boldsymbol{f}_\sigma \tag{49}$$

where $F_{\rho \mathbf{v}}$ is the mass flux defined as:

$$F_{\rho \mathbf{v}} = (\rho \mathbf{v})_f \cdot \mathbf{S}_f \tag{50}$$

The mass flux can be calculated as a function of the limited fluxes of α_m and α_b as follows (Supplementary Material, Appendix A, Identity 6):

$$F_{\rho \mathbf{v}} = \rho_a F_{\mathbf{u}} + (\rho_b - \rho_w) F_b^{\lim} + \left[\left(\rho_{m,f} - \rho_a\right) - \frac{\alpha_b}{\alpha_m}(\rho_b - \rho_w)\right] F_\gamma^{\lim}. \tag{51}$$

After the time discretization, Eq. (49) can be written as a system of linear equations as follows:

$$\mathbf{A}\mathbf{v} = \mathbf{r} - \nabla p_{rgh} - \mathbf{g} \cdot \mathbf{x} \nabla \rho + \boldsymbol{f}_\sigma \tag{52}$$

Eq. (52) is solved by using the previous value of p_{rgh}, obtaining a predicted value of the velocity ($\mathbf{v}^*$). Splitting $\mathbf{A}$ into its diagonal ($\mathbf{A}_D$) and off-diagonal ($\mathbf{A}_{LU}$) components, Eq. (52) can be rewritten as:

$$\mathbf{A}_D \mathbf{v} = \mathcal{H}(\mathbf{v}) - \nabla p_{rgh} - \mathbf{g} \cdot \mathbf{x} \nabla \rho + \boldsymbol{f}_\sigma \tag{53}$$

where

$$\mathcal{H}(\mathbf{v}) = \mathbf{r} - \mathbf{A}_{LU} \mathbf{v} \tag{54}$$

$\mathbf{A}_D$ is easily invertible, and therefore the velocity can be written as

$$\mathbf{v} = \mathbf{A}_D^{-1} \mathcal{H}(\mathbf{v}) - \mathbf{A}_D^{-1}\left[\nabla p_{rgh} + \mathbf{g} \cdot \mathbf{x} \nabla \rho + \boldsymbol{f}_\sigma\right] \tag{55}$$

Eq. (55) can be substituted in (8), and $\mathbf{v}$ approximated with $\mathbf{v}^*$, yielding to

$$\nabla \cdot \left[\mathbf{A}_D^{-1} \mathcal{H}(\mathbf{v}) - \mathbf{A}_D^{-1}\left(\nabla p_{rgh} + \mathbf{g} \cdot \mathbf{x} \nabla \rho + \boldsymbol{f}_\sigma\right)\right] = \nabla \cdot \left[\gamma(1-\gamma)\frac{\rho_\gamma - \rho_a}{\rho} \mathbf{u}_{\gamma-g} + \alpha_b s \frac{\gamma - \alpha_b}{\gamma + \alpha_b s} \frac{\rho_\gamma}{\rho} \mathbf{v}_{b-w}\right]. \tag{56}$$

Reorganizing (56), the pressure equation is obtained:

$$\begin{aligned} \nabla \cdot \left(\mathbf{A}_D^{-1} \nabla p_{rgh}\right) = \nabla \cdot \Big[& \mathbf{A}_D^{-1} \mathcal{H}(\mathbf{v}^*) - \mathbf{A}_D^{-1} \mathbf{g} \cdot \mathbf{x} \nabla \rho - \mathbf{A}_D^{-1} \boldsymbol{f}_\sigma \\ & - \alpha_m (1 - \alpha_m) \frac{\rho_m - \rho_a}{\rho} \mathbf{u}_{m-g} - \alpha_b s \frac{\alpha_m - \alpha_b}{\alpha_m + \alpha_b s} \frac{\rho_m}{\rho} \mathbf{v}_{b-w} \Big] \end{aligned} \tag{57}$$

The algorithm iterates between Eqs. (55) and (57) until convergence is reached. After convergence, the values of volume-averaged velocity flux ($F_{\mathbf{u}}$) are updated from the mass-averaged velocity flux ($F_{\mathbf{v}}$):

$$F_{\mathbf{u}} = F_{\mathbf{v}} - \left[\alpha_m (1 - \alpha_m) \frac{\rho_m - \rho_a}{\rho}\right]_f F_{m-g} - \left[\alpha_b s \frac{\alpha_w}{\alpha_m + \alpha_b s} \frac{\rho_m}{\rho}\right]_f F_{b-w} \tag{58}$$

4.3. Calculation of the source term

The term that transforms continuous air into bubbles (S_b^+) is calculated using the same expression as in Eq. (30), but considering some limiters to avoid numerical instabilities. The first limiter avoids that α_b grows beyond 0.9 at the interface. The second limiter provides a bound for the source term by the amount of continuous air in the cell.

Because S_b^+ is a transfer term, the amount of bubbles created in a cell has to be smaller or equal to the amount of continuous air present on the cell. Then S_b^+ is calculated as:

$$S_b^+ = \min\left[\frac{0.9}{\delta t}H(0.9-\alpha_b), \frac{0.9-\alpha_b}{\Delta t}, \frac{\alpha_a}{\Delta t}\right]\xi_1 \tag{59}$$

To calculate δt and ξ_1 it is necessary to specify the value of δs. In contrast to the theoretical model, in an algebraic VOF, the free surface is not defined as a surface but as a sharp transition of α_m from 1 to 0 (usually contained within 2 or 3 cells). The definition of $N_{\mathrm{FS},1}$ (and $N_{\mathrm{FS},2}$) has to be adapted accordingly. $N_{\mathrm{FS},1}$ is defined in the numerical model as the set of cells in the transition region surrounding the area of $\alpha_m = 1$ (i.e the first cell in the transition of α_m form 1 to 0). ξ_1 is then calculated based on the values of α_m at the cell and its neighbors ($\alpha_{m,N}$) as:

$$\xi_1 = \begin{cases} 1 & \alpha_m < 1 \wedge \alpha_{m,N} = 1 \wedge \alpha_{b,N} < 0.9 \\ 0 & \text{otherwise} \end{cases} \tag{60}$$

The combination of the first and second condition indicates that the cell corresponds to the first cell in the transition region. The third condition avoids an unlimited growth of the bubble region by only activating the source term when enough bubbles are transported into the flow. This formulation not only restricts the transformation of air into bubbles to a thin region, but also maintains the interface sharp while growing. Because δt is a function of δn, which depends on the cell size, in the numerical implementation, δt is reformulated based on the CN defined as:

$$\delta t = \frac{\Delta t}{\mathrm{CN}}. \tag{61}$$

The term that transforms bubbles into continuous air (S_b^-) is calculated as:

$$S_b^- = \min\left[\frac{0.9}{\delta t}H(\alpha_b), \frac{\alpha_b}{\Delta t}\right]\xi_2 \tag{62}$$

where ξ_2 is equal to 1 in the last cell of the transition region of α_m, and it is calculated as:

$$\xi_2 = \begin{cases} 1 & \alpha_m < 1 \wedge \alpha_{m,N} = 0 \\ 0 & \text{otherwise} \end{cases} \tag{63}$$

This approach for the calculation of ξ_2 was implemented to maintain the interface region sharp during a process of degassing.

5. Model verification and validation

The model is verified and validated using four experimental cases which test different aspects of the formulation. The first test is a two-dimensional degassing tank. It corresponds to an enclosed tank partially filled with water in which bubbles are released to the continuous air region. For this test, no experimental data exist, but it is useful as a verification tool. The second test corresponds to the experiments of Friedl and Fanneløp [61]. Their experiments represent a bubble plume interacting with the free surface. The third case corresponds to a plunging jet tested by Chanson et al. [14] for which air concentration profiles are available. For the fourth and last test, a set of experiments performed over stepped spillways by Amador [62] and by Felder and Chanson [10] are simulated.

5.1. Degassing of a tank

The test set-up consists of a two-dimensional tank partially filled with water and bubbles. The bubbles are located in a circular region in the center of the domain (Fig. 5). The tank is 0.2 m high and 0.1 m wide. The free surface is located 0.15 m over the bottom. The tank depth is arbitrarily set as 0.1 m (this value does not affect the results of the two-dimensional simulation, but it is used for the calculation of volumes). The circular bubbly region has a diameter of 0.06 m, and its center is located 0.075 m above the bottom. The bubble phase fraction in this region is $\alpha_b = 0.4$. The density of water and air are specified as 1000 kg/m^2 and 1.225 kg/m^2 and the kinematic viscosity as 1×10^{-6} m^3/s and 1.48×10^{-5} m^3/s, respectively. The surface tension of water-air is set equal to 0.07 N/m. These parameters are used throughout all simulations. The boundaries of the tank are represented as walls, forming a closed system where the total mass is maintained constant. At the walls, the velocity is set to zero, the pressure

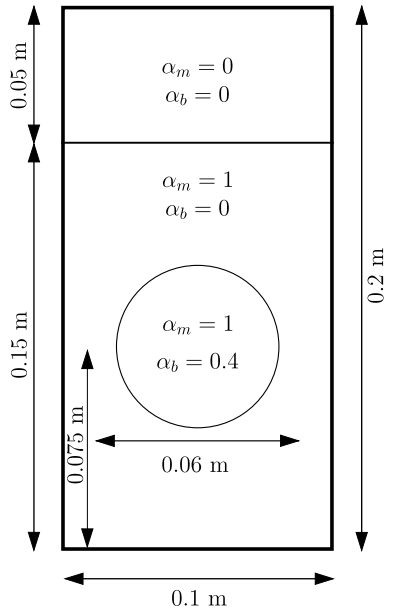

Fig. 5. Geometry and initial conditions for the tank degassing test.

gradient is set such that the flux on the boundary is that specified by the velocity Boundary Condition (BC), and the rest of the variables are set with zero-valued Neumann BCs. The $k-\epsilon$ model is employed to represent the Reynolds stresses. Wall functions are used as BC for k and ϵ. The same type of BCs are used at wall boundaries throughout all simulations. The mesh consists of rectangular elements of 0.6 mm by 0.5 mm ($N_x \times N_z = 150 \times 400$). Null velocity and hydrostatic pressure are defined as initial conditions. Second-order schemes are used for space discretization, and an interface compression scheme is used for the interpolation of $\mathbf{u}_{m-a}$ [63]. ϕ is set to zero in the whole domain. The turbulent Schmidt number is set to $Sc = 10^6$ to avoid any type of diffusion and C_α is set to 1.

When the simulation begins, air bubbles are transported upwards due to buoyancy until they travel across the free surface and are incorporated into the continuous air. When the bubbles become continuous air, the free surface (defined as the location where $\alpha_m = 0.5$) lowers proportionally to the amount of bubbles leaving the water-bubble mixture. Even though there is no experimental data to validate this case, it is useful to verify the following aspects of the code:

- Because the system is closed, the amount of mass of air (bubbles and continuous air) and water should remain constant throughout the simulation.
- The reduction of free surface height should be proportional to the volume of bubbles released.
- By using a mesh fine enough such that the reduction in free surface height encompasses several elements, we can verify that the numerical method maintains the interface sharp during its descent.

In order to verify grid independence of the numerical results, we present in Fig. 6 (left) the temporal evolution of the total volume of bubbles in the domain, obtained with the use of three meshes of $N_x \times N_z$ equal to 75×200; 150×400 and 300×800. The results are virtually the same, showing that with any of those meshes, the same results are achieved.

The evolution of the volume occupied by each phase in the domain is presented in Fig. 6 (right). At the beginning of the simulation, the total volume occupied by each phase can be calculated using simple geometrical considerations. At $t = 0$, the volume-integrated values of water-bubble mixture, water, bubble, and air phase fractions are 1.5×10^{-3} m^3, 1.39×10^{-3} m^3, 0.11×10^{-3} m^3 and 0.5×10^{-3} m^3, respectively. At $t = 0.2$ s, the bubbles start to reach the free surface and get transformed into continuous air. The reduction in α_b implies an equal reduction of α_m. After $t = 0.5$ s, most of bubbles have been transformed into continuous air and the total

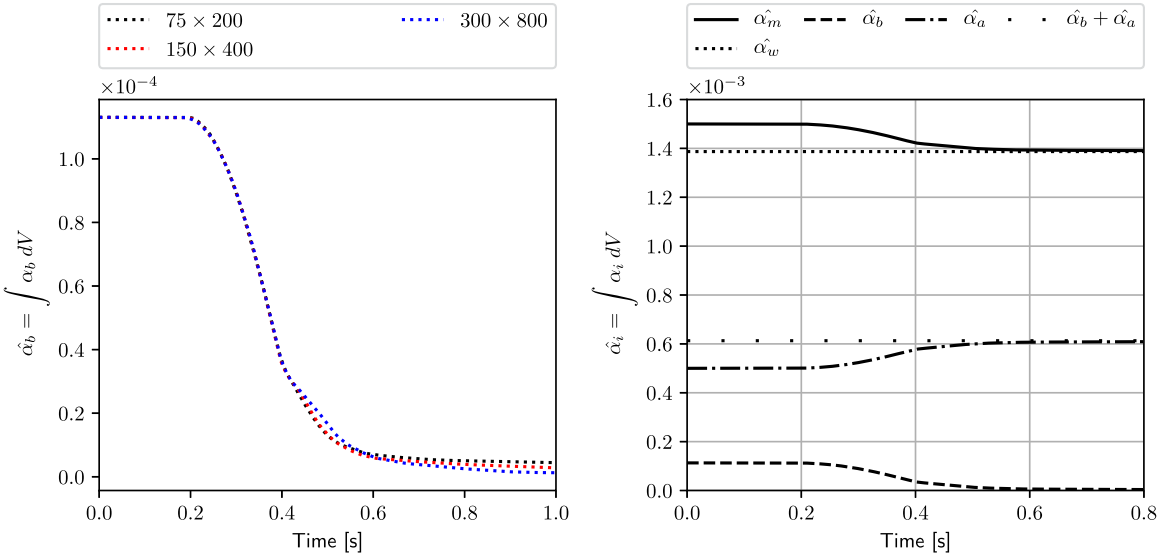

Fig. 6. Left: Evolution of the total volume of dispersed air (bubbles) over time obtained with three different meshes. Right: Temporal evolution of continuous air, dispersed air (bubbles), total air, water, and water-bubble mixture total volume over time.

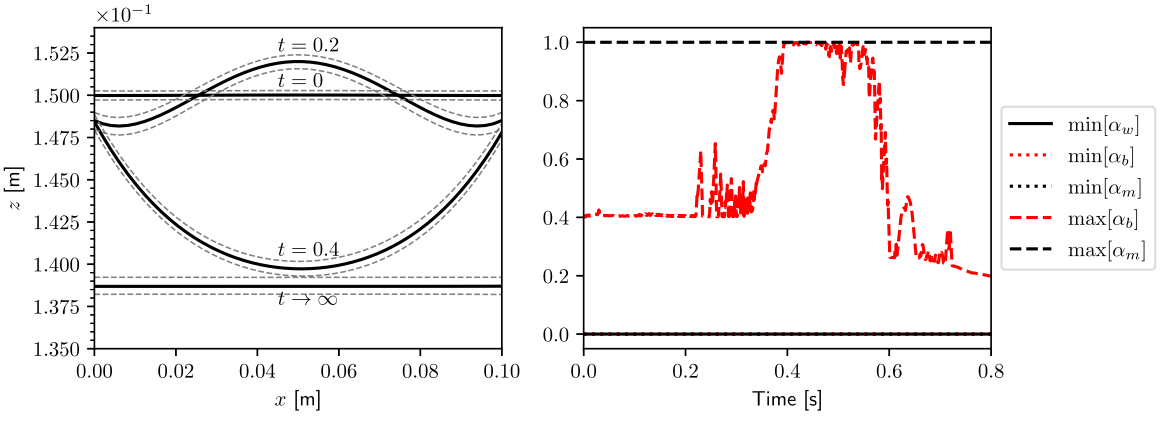

Fig. 7. Left: Evolution of free surface location over time. The solid lines represent the iso-surface of $\alpha_m = 0.5$ and the dashed lines indicate the iso-surfaces of $\alpha_m = 0.1$ (top) and $\alpha_m = 0.9$ (bottom). Right: Minimum and maximum values of α_m, α_b and $\alpha_w = \alpha_m - \alpha_b$ over the entire domain.

volume occupied by each fraction remains almost constant. Over the duration of the simulation, the total amount of water ($\hat{\alpha_w} = \int \alpha_w dV$) and the total amount of air ($\hat{\alpha_b} + \hat{\alpha_a} = \int (\alpha_b + \alpha_a) dV$) remained constant.

To evaluate how effective the algorithm proposed in Section 4.1 is in guaranteeing the three required properties (enumerated in Section 4.1), the minimum and maximum values of α_m, α_b and $\alpha_w = \alpha_m - \alpha_b$ over the entire domain are presented in Fig. 7 (right). The values of phase fractions remain bounded throughout the simulation. The water and mixture fraction reach minimum values of the order -1×10^{-12} while the bubble fraction reaches values of the order of -1×10^{-8}. These errors arise from the tolerance imposed in the solution of the pressure equation (which leads to small errors in continuity). A reduction in the tolerance of the solution of the pressure equation leads to a reduction in this type of errors. A similar behavior is presented for the maximum values of α_m and α_b.

The iso-surfaces of $\alpha_m = 0.5$ at $t = \{0, 0.2, 0.4\}$ s and $t \to \infty$ are presented in Fig. 7 (left). The dashed lines around the solid lines represent the iso-surfaces of $\alpha_m = 0.1$ (top) and $\alpha_m = 0.9$ (bottom), indicating the scatter of this parameter during the free-surface descent. On the vertical axis, the minor tick represents the cell height. The reduction of height is consistent with the geometrical considerations mentioned before. The deformation of the free

surface at $t = 0.2$ s occurs due to the velocity field generated by the bubbles' ascent in the tank (no bubble was released at this time). At $t = 0.4$ s, more than 50% of the bubbles were transformed into continuous air, which can be noted in the location of the free surface. After all bubbles were released, the free surface experiences lateral oscillations which eventually damp, ending with a flat free surface at $z = 0.139$ m. The dashed lines show that the free surface remains constrained within two cells over the simulation, showing that the algorithm is capable of maintaining a sharp interface even during an abrupt motion of the free surface (caused by the elimination of bubbles) that encompasses several cells (22 cells for this test).

5.2. Bubble plume interacting with the free surface

Friedl and Fanneløp [61] tested experimentally a bubble plume formed in a mid-size water tank. This phenomenon also occurs in natural undersea gas releases and blowouts in offshore drilling [64]. It is also used as a mechanism to improve water quality in reservoirs and lakes or to prevent the formation of ice on the free surface. The main goal of this test is to evaluate the interaction of the bubble phase with the free surface [65].

Air released from the bottom breaks up into bubbles that move upwards due to buoyancy, as the plume expands laterally. When the bubbles reach depths smaller than the plume radius, water in the plume gets deflected laterally, interacting with the free surface; this causes an elevation of the surface known as fountain [66]. Fountain shapes are well represented by a Gaussian curve $\hat{h}(r)$ given by:

$$\hat{h}(r) = h_f e^{-r^2/b_f^2} \tag{64}$$

where h_f is the elevation at the center of the fountain and b_f is the width of the fountain.

The experiments selected herein correspond to the case a4 by Friedl and Fanneløp [61], and were performed in a square section tank with a side length of 1 m. The water depth was set at 0.66 m. The air was injected from the bottom through a square duct of 0.022 m side at a speed of 2.6 m/s. The relative velocity between water and air v_{b-w}^{∞} was set to 0.35 m/s based on the experimental results. The numerical model was set up using a quarter of the domain and establishing symmetry BCs on the symmetry planes. At the bottom of the tank, on the intersection of the symmetry planes, the inlet BC was set with an area of a quarter of the original inlet, a constant upward velocity and bubble phase fraction of $\alpha_b = 1$. On the sides and on the rest of the bottom part of the domain, wall BCs were set. On the top boundary of the domain, a total pressure of zero was established, and a mixed BC for the rest of the variables were used: a Neumann BC was used if the flow is exiting the domain and a Dirichlet BC if the flow is entering the domain. The mesh consisted of 704,518 cubic cells, with side dimensions ranging from 1.2 cm to 3 mm. Mesh refinements were concentrated in the region encompassing the plume and near the free surface. Grid independence was verified for the presented mesh (not shown herein). The $k - \epsilon$ turbulent closure was used. ϕ is set to zero in the whole domain. The turbulent Schmidt number is set to $Sc = 0.5$ and $C_\alpha = 1$.

The shape of the free surface after the simulation reaches steady state is presented in Fig. 8(a) with the Gaussian curve calculated using the parameters reported by Friedl and Fanneløp [61] for the case a4: $h_f = 0.038$ cm and $b_f = 0.101$ cm. The results obtained by Marquéz Damián and Nigro [36] using a pure VOF model and a RANS closure are also presented on the same figure. The model predicts reasonably well the fountain's height and width. The shape of the two curves differs slightly near $r/b_f \approx 1.75$. The experimental result shows a smooth transition to the horizontal portion of the curve with $\hat{h} \to 0$, while the numerical model predicts a slight dip before the horizontal portion of the curve as well as a uniform value below 0. The experimental curve shown in Fig. 8 is not the representation of the exact measurements, but a Gaussian curve fitted to them (only this was reported by Friedl and Fanneløp [61]); therefore, some differences between the numerical model and the curve are expected, and within the experimental uncertainties.

The proposed model presents a more accurate description of the height and width of the fountain than the pure VOF model. The VOF model is limited by the dimensions of cells and the turbulence closure. The flow structures that lead to the break up of the plume into smaller bubbles and then transported laterally are not present in this RANS simulation, and therefore it is expected that the width of the fountain would be underpredicted. Furthermore, the sharpness of the interface in pure algebraic VOF is compromised when features of the order of the cell dimensions are present [54]. This leads to unphysical rising velocities of the air phase that can affect the height of the fountain. The proposed model is capable of representing this phenomenon with better accuracy than a pure VOF and RANS closure model with a much lower computational cost.

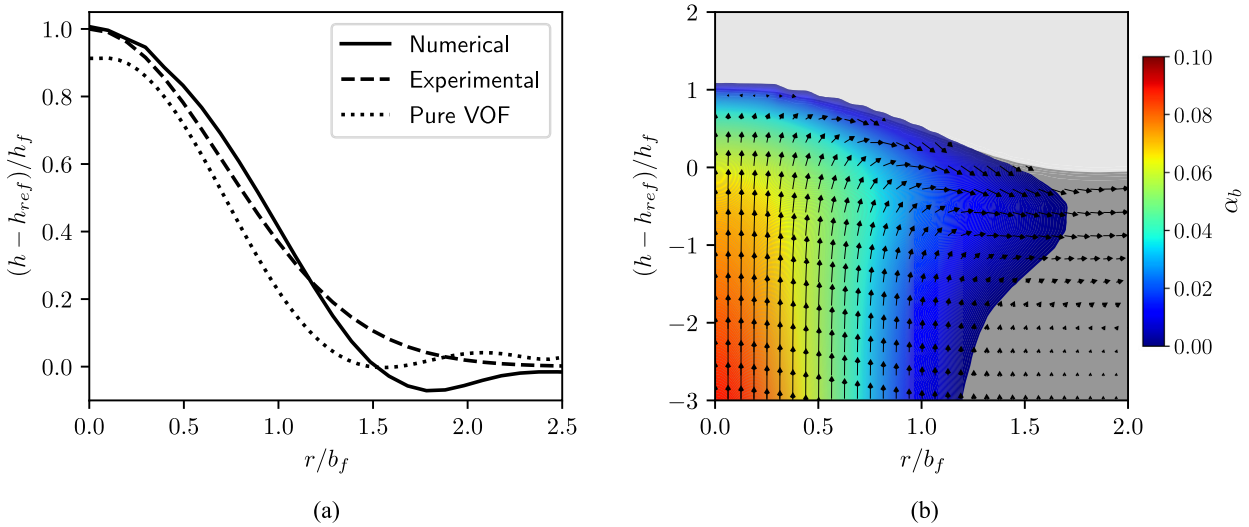

Fig. 8. (a): Free surface position for Friedl and Fanneløp [61] experiment obtained with the proposed model, pure VOF [36], and theoretical model (Gaussian curve). (b): Distribution of α_m (saturated at $\alpha_m = 0.5$) superimposed with velocity vectors on the fountain region.

The distribution of α_b and of α_m superimposed with velocity vectors on the fountain region is presented in Fig. 8(b). The bubble plume is deflected laterally near the free surface, following the description of the flow provided by Friedl and Fanneløp [61] and by their Fig. 2. This shows that the model can reproduce the main characteristics of the flow dynamics and the interaction of the bubble plume with the free surface. Unfortunately, there is no further quantitative data other than the free surface location (such as bubble concentration or flow velocity) to validate this experiment.

5.3. Plunging jet

The third test corresponds to the vertical plunging jet experiments performed by Chanson et al. [14]. When a jet impinges into a body of water at a sufficiently high velocity, air becomes entrapped in the impingement point and carried by the flow into the water body. Plunging jets occur in nature (e.g., waterfalls), man-made structures (e.g., ski jump buckets) as well as industrial applications (e.g., re-oxygenation weirs). The experiment corresponds to the Model 1 of Chanson et al. [14] and possesses an impact velocity of $V_1 = 3.5$ m/s. The experimental setup consists of a jet nozzle with a diameter of $D = 0.025$ m and a channel 0.3 m wide and 1.8 m deep. The distance between the nozzle and the undisturbed free surface is $z_1 = 0.1$ m. Air concentration profiles were measured at $z/D = 1.6$, 2.5 and 4.1 ($z = 0$ corresponds to the free surface). A picture from the experiment for a different case with similar Froude number (Model 2, $V_1 = 3.3$ m/s) extracted from Chanson et al. [14] is presented in Fig. 9(a) (no photo of the selected case was available).

The numerical model was set up using a two-dimensional domain and wedge BCs to represent the axial symmetry of the experiment (see Fig. 9(b)). This simplification does not compromise the accuracy of the solution and significantly reduces the computational cost of the simulation [67]. The mesh is locally refined in the regions of interest: the jet, the impingement region, and the bubble plume region. It consists of squared cells of 0.1 mm side in the impingement region and 0.2 mm in the jet and in the bubble plume. Mesh independence of the results was verified for the presented mesh (not shown herein). The standard $k-\epsilon$ turbulence closure was used. The inlet velocity is calculated based on the impact velocity using Bernoulli's principle, and turbulence parameters were approximated following Lopes et al. [22]. On the top boundary of the domain, a total pressure of zero is set and a mixed BC is used for the rest of the variables. Wall BCs were implemented for the bottom and lateral walls. A small outlet far from the region of interest was implemented such that the average water level on the tank is maintained constant (i.e. the volume of water entering the domain through the inlet equals the volume of water leaving the domain through the outlet). This BC does not affect the main features of the flow because the bubbles do not reach positions near the

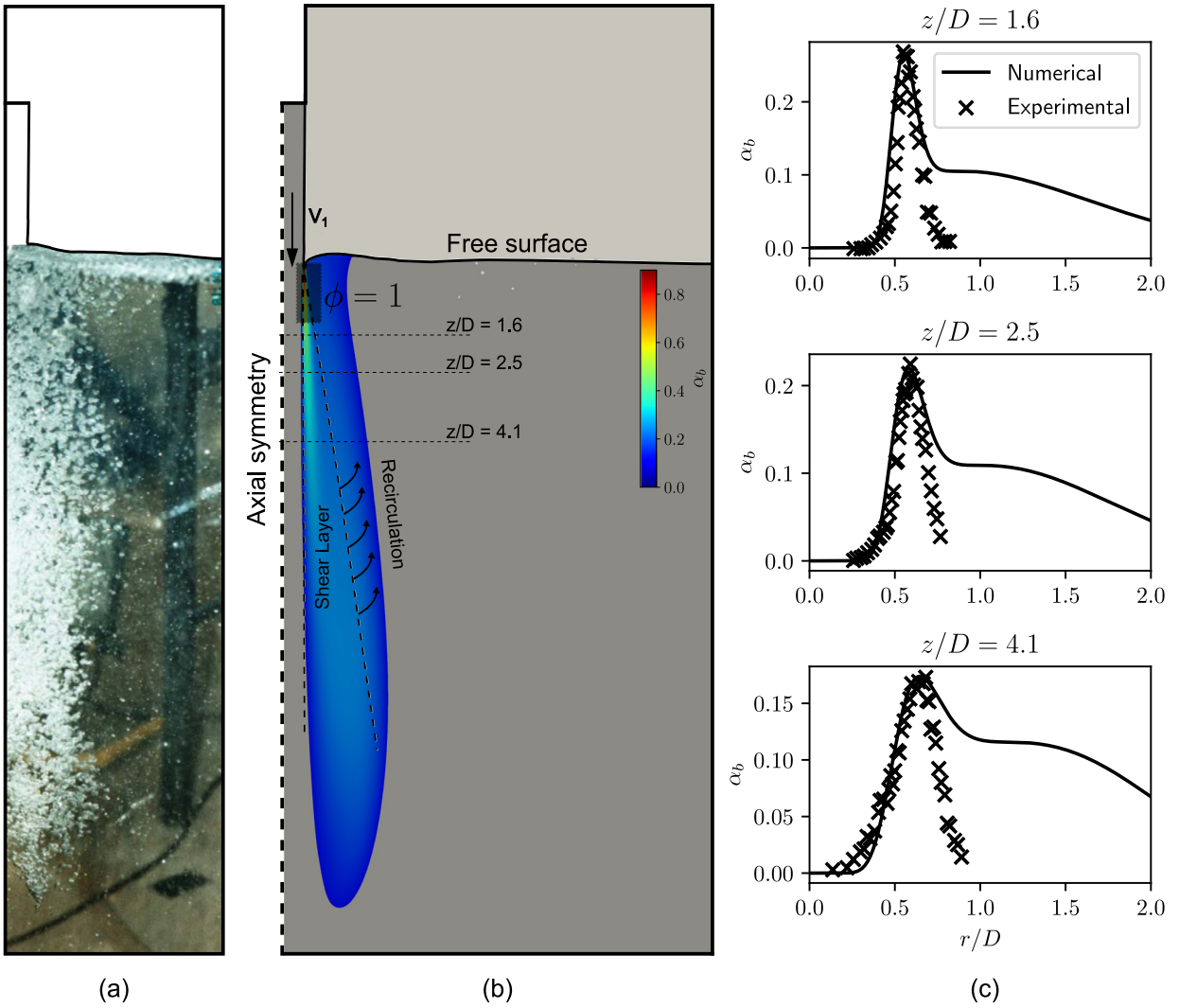

Fig. 9. (a): Picture from the experiments by Chanson et al. (extracted from [14]). (b): Distribution of α_b, superimposed with α_m (saturated at $\alpha_m = 0.5$) obtained with the numerical model. (c): Numerical results of α_b profiles compared to experimental values.

outlet, and the outlet velocity is small (4.8×10^{-4} m/s). The air entrainment model was activated ($\phi = 1$) in a small region near the impingement region as indicated in Fig. 9(b). Second-order schemes were used for space discretization and first-order for time discretization. The bubble diameter was set to 1 mm, the turbulent Schmidt number to $Sc = 10$ and $C_\alpha = 1$. This Schmidt number value is clearly higher than the majority of values reported in the literature [68]. However, it is easy to explain based on recent published experience: Incompressible single-phase turbulent closures that do not take into account effects of buoyancy, lead to the overproduction of turbulent kinetic energy at the free surface [69,70]. This leads to the overprediction of ν_T and of the bubble turbulent diffusivity. This effect has to be compensated with a high value of Sc. More appropriate turbulent closures that account for buoyancy effects and the modulation of turbulence caused by bubbles will be studied in future work.

The distribution of α_b, superimposed with α_m, obtained with the numerical model is presented in Fig. 9(b). A visual inspection of the numerical results and the experiment photo reveals similar distributions of bubbles (we recall that the picture does not correspond to the exact experiment as the one simulated, but to a similar one, and therefore, all comparisons with this picture are only qualitative). Air concentration is higher at the impingement point and bubbles are advected vertically into the tank. As bubbles transfer their downward momentum and become diffused laterally, the buoyancy effects become dominant, and bubbles start to travel upwards, forming a recirculation effect.

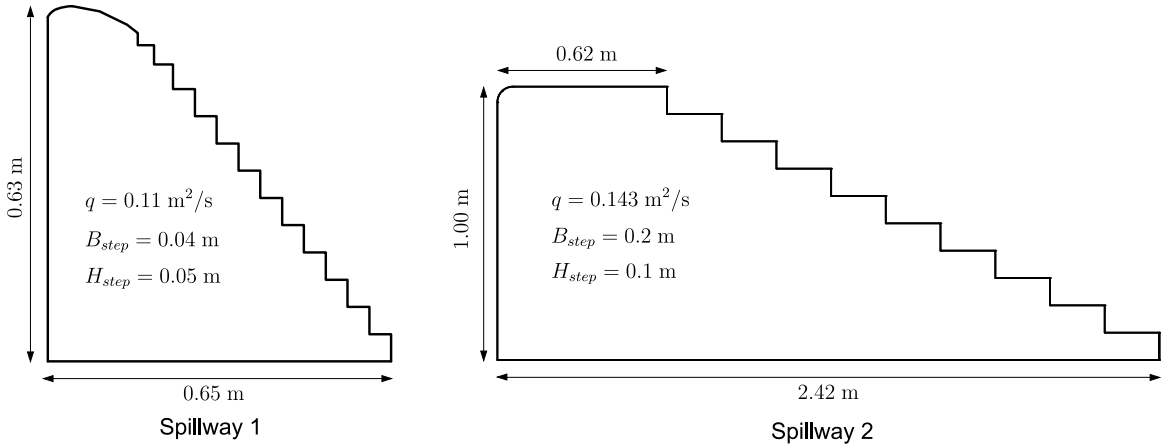

Fig. 10. Geometry for spillways 1 and 2.

The comparison between the distribution of α_b obtained numerically with the experimental data at $z/D = 1.6$, 2.5 and 4.1 is displayed in Fig. 9(c). The model accurately describes the peak concentration and general bubble distribution. The concentration profile shows a discrepancy between numerical and experimental results for $r/D \geq 1$. The experimental data tends to zero, while the numerical data shows a more uniform distribution of α_b with values close to 0.1. The experimental data would seem to be considering only the bubbles in the air diffusion layer but not the ascending ones. From the experiment's photo, it is clear that a significant amount of bubbles are present for $r/D \geq 1$. Furthermore, the momentum shear layer tends to be wider than the air diffusion layer [14], and therefore the experimental distribution of bubbles would not fulfill continuity with this type of bubble distribution.

5.4. Stepped spillway

The flow over stepped spillways for the skimming flow regime is characterized by a coherent stream of water moving over the steps, and interacting with the recirculating fluid in between cavities [71]. The skimming flow presents two clearly distinct zones: the non-aerated region, starting at the crest of the spillway with a smooth profile, followed by small disturbances; and the aerated region, beginning at the inception point (region where air entrainment begins), which is characterized by high amounts of air entrained into the flow. It is widely accepted that air entrainment occurs when the turbulent boundary layer reaches the free surface, and turbulent eddies are energetic enough to disturb it [53,72–75]. Zabaleta et al. [76] linked the onset of air entrainment with turbulent flow structures reaching the free surface with enough frequency, which proved to be highly correlated with the growth of the boundary layer.

To validate the model, the experiments of Amador [62] were used for the non-aerated region, and the experiment of Felder and Chanson [10] for the aerated counterpart. Amador [62] conducted the experiments in a rectangular stepped spillway of 0.5 m wide, 2.0 m high, and steps of 5 cm high and 4 cm wide. The first three steps had variable dimensions, emulating the geometry of a WES crest profile. The discharge per unit length was 0.11 m^2/s. Velocity measurements were performed using Particle Image Velocimetry (PIV). The experiments of Felder and Chanson [10] were performed in a rectangular stepped spillway 1.0 m wide, 2.0 m long, and 0.9 m high. The steps were 10 cm high and 20 cm wide. In this study, the experiment corresponding to a unit discharge of 0.143 m^2/s was simulated. Air concentration was measured using a double-tip conductivity probe. A schematic diagram of the two spillways with the main dimensions is presented in Fig. 10. Integer values represent the outer edge of the steps (e.g., 6), while half values represent the inner position between steps (e.g. 6.5). In the rest of this article, the spillway used by Amador [62] will be referred to as 'spillway 1' while the one used by Felder and Chanson [10] will be referred to as 'spillway 2'.

The flow over both spillways is represented on two-dimensional domains with similar mesh resolutions and BCs. The domains include the approximation region upstream of the crest and 13 and 10 steps for spillways 1 and 2, respectively (only the non-aerated region was represented for spillway 2). The velocity at the inlets was specified

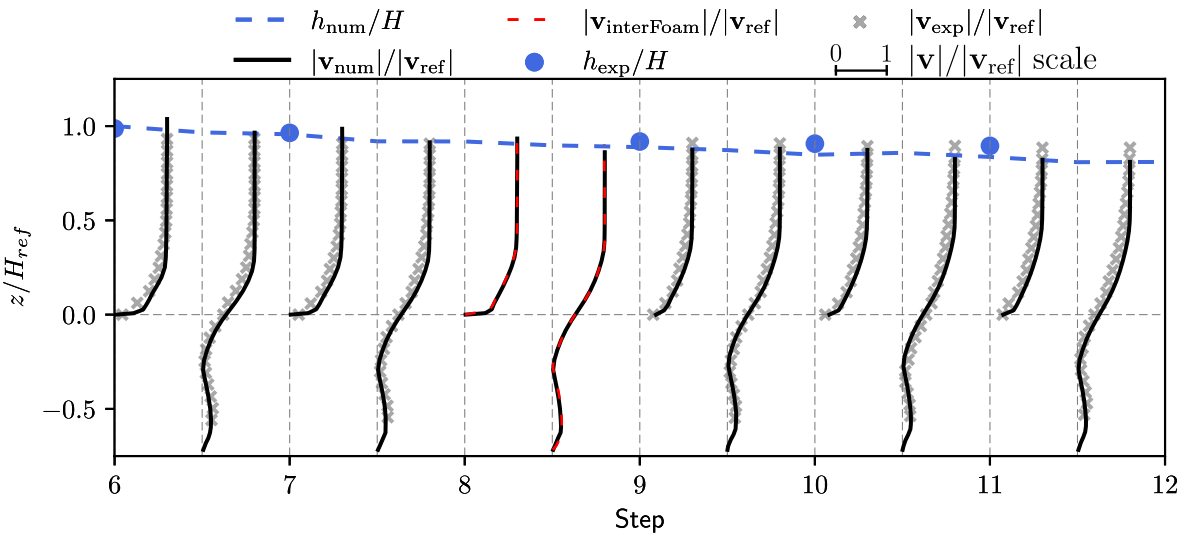

Fig. 11. Numerical results of velocity profiles (black solid lines) and free surface elevation (blue dashed line) compared to experimental velocity profiles (gray cross symbols) and measured free surface elevation (blue circles) from Amador [62] for the non-aerated region. The dashed red lines represent the numerical results obtained by Toro et al. [79].

based on the flow rates, whereas for the outlet boundary an advective BC was used. For the walls, similar BCs as the ones used for previous simulations were employed. For the top boundary, the same BCs as presented in the bubble plume case (Section 5.2) were employed. For spillway 1, the mesh consisted of 39.000 cells; for spillway 2, 109.066 cells were used. In both cases, this number of cells resulted in similar cell dimensions for both spillways (2.5 mm) as well as similar values of y^+ (within 30 and 60). Grid independence was verified for the presented meshes (not shown herein). Second-order schemes were used for space discretization, and an interface compression scheme was used for the interpolation of $\mathbf{u}_{m-a}$. In both cases, the time step was limited by the condition $CN \leq 0.5$. The RNG $k-\epsilon$ model was used for the turbulence closure of both spillways. The turbulent Schmidt number is set to $Sc = 10$ in spillway 2, and $C_\alpha = 1$ in both spillways. Similar considerations regarding the Schmidt number and the turbulent closure as mentioned in Section 5.3 apply to this case.

The main goal of the simulation of the non-aerated region is to show that in the absence of bubbles, the model recovers the traditional VOF formulation for segregated flows, and can accurately simulate the non-aerated portions of the flow. Water depths and velocity profiles obtained with the numerical model, as well as reported from the experiments, are presented in Fig. 11 (water depth was only reported for steps 6 and 7 and 9 to 11, and velocity profiles were reported for the same steps and for intermediate locations). The z-coordinate is measured perpendicular to the pseudo-bottom and it has its origin at it. Velocity profiles, as well as water level, show satisfactory agreement with the experimental data. The model slightly underpredicts the water level in steps 9 to 11, but the difference between measured and modeled values is below 3% for most of the points, well within the experimental uncertainty. The velocity profiles over the step edges (integer values of steps) follow a power law, agreeing with the analyses of other authors [77,78]. The differences between measured and modeled velocity magnitudes are below 5% for all the profiles. Toro et al. [79] employed the VOF solver already implemented in the OpenFOAM platform, interFoam [52], to simulate spillway 1. The velocity profiles in steps 8 and 8.5 obtained with the proposed model (black, solid lines) superimposed with the obtained by Toro et al. [79] (red, dashed lines) are presented in Fig. 11. Both simulations presented almost identical results, showing that both models are virtually identical in the absence of dispersed air.

To simulate spillway 2, the air entrainment model was activated ($\phi = 1$) downstream of an intermediate section in between steps 5 and 6, based on the experimental results (this method was adopted herein for simplicity, but we will follow a more detailed procedure [53] in the near future). A bubble diameter of 1 mm was employed to calculate the slip velocity between water and air. The distribution of the water-bubble mixture superimposed with the bubble phase distribution is presented in Fig. 12. The air starts to be gradually incorporated into the flow between steps 5 and 6. The free surface increases as air is incorporated, and bubbles penetrate deeper into the flow as we

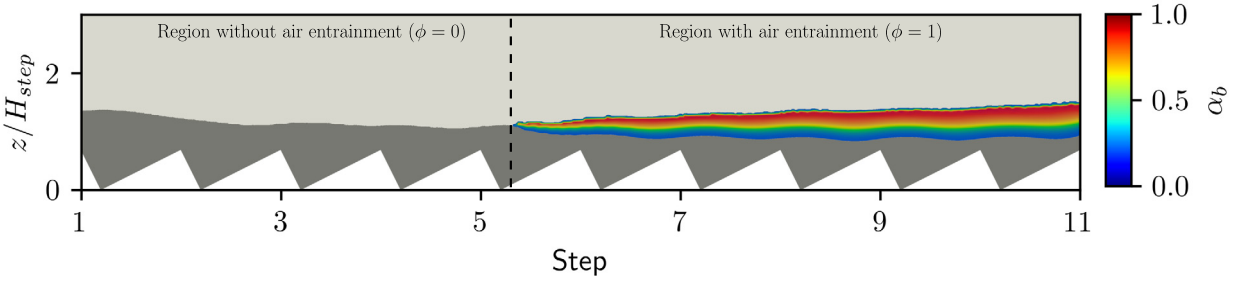

Fig. 12. Bubble phase distribution (red to blue scale) superimposed with α_m distribution (grayscale, saturated at 0.5).

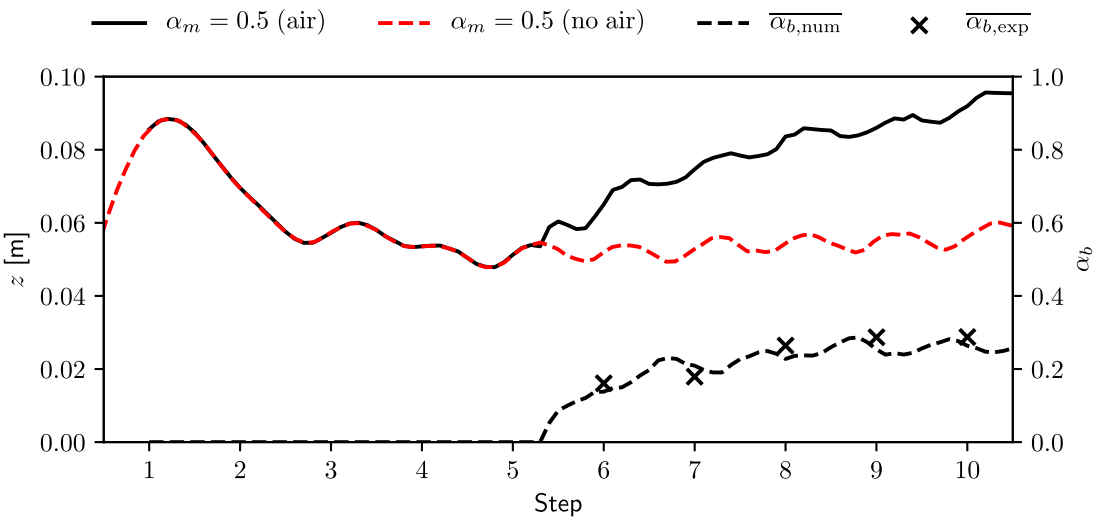

Fig. 13. Iso-surfaces of $\alpha_m = 0.5$ for spillway 2, obtained with the air entrainment model activated (solid black line) and without the air entrainment model (dashed red line). Values of mean air concentration obtained with the numerical model (dashed black line) and from the experiments of Felder and Chanson [10] (black cross symbols).

move downstream. The highest concentrations of bubbles are present near the surface with values close to 0.9 and decrease deeper into the flow. The concentration profiles present a modulation with a wavelength similar to the step's separation due to the different distribution of ν_t within the steps.

The comparison between free surface location (iso-surface $\alpha_m = 0.5$) for the model with and without air entrainment as well as mean air concentrations are presented in Fig. 13. Mean air concentration is calculated using the traditional formulation for self-aerated flows [3] as follows:

$$\overline{\alpha}_b = 1 - \frac{d_w}{Z_{90}}; \quad d_w = \int_0^\infty \alpha_w \, dz \tag{65}$$

where d_w is the equivalent water depth and Z_{90} is the height at which $\alpha_b = 0.90$. The measured and simulated values of mean air concentration show very good agreement. Before step 5, both simulations show exactly the same results: water depth decreases as we move downstream due to the acceleration of the flow. In between steps, water level presents a wavy pattern that scales with the step's separation. After the inception point, mean air concentration begins to increase as well as the free surface for the simulation with air. As $\overline{\alpha}_b$ increases, the difference between the simulations with and without air becomes more significant. At step 10, the simulation with air shows an over 40% increase with respect to the simulations without air. This is a testament to why using a model that can accurately reproduce bulking is so important for the simulation of open-channel, self-aerated flows. When air concentrations are important, representing the bubble phase as a passive scalar that does not affect the depth of the flow leads to important deviations from reality.

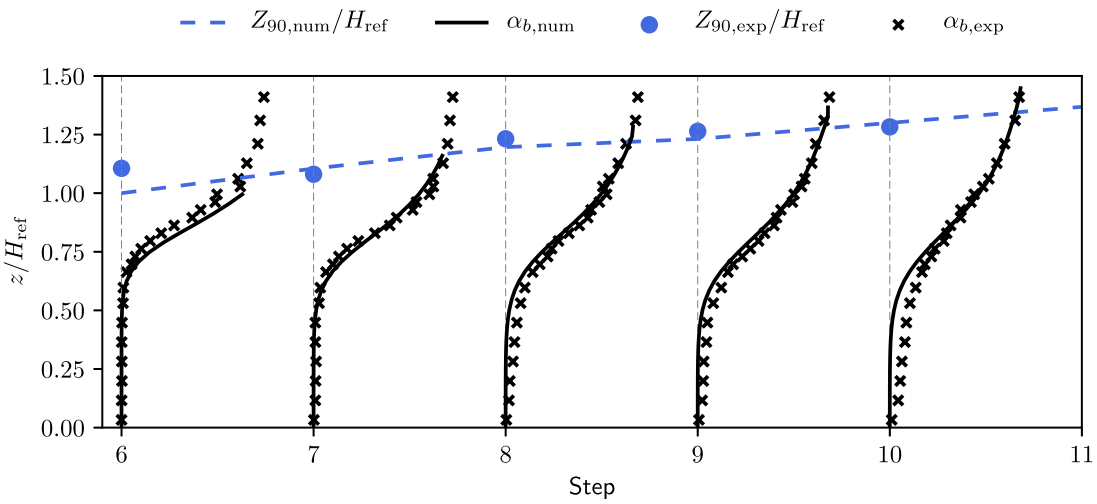

Fig. 14. Z_{90} profile and velocity profiles for spillway 2 obtained with the numerical method compared to values obtained experimentally by Felder and Chanson [10], pertaining to the aerated region.

The comparison of Z_{90} between numerical and physical model, as well as profiles of concentration of bubbles, are presented in Fig. 14. Air concentration profiles follow the traditional shape of a hyperbolic tangent function. The air concentration has a value close to 0.9 near the free surface (by definition), and quickly decreases closer to the pseudo-bottom. In step 6, α_b has significant values only on the top 25% of the water depth, while in step 10, the bubbles reach over 50% of the flow depth. Numerical and experimental bubble concentration show very satisfactory agreement, especially in the regions near the free surface. A slight difference between measured and simulated concentrations in the regions close to the pseudo-bottom can be noticed. Because bubble diffusivity is proportional to the eddy diffusivity (which is low close to the pseudo-bottom), and the slip velocity magnitude is higher in low concentrations, these results were expected. The overproduction of turbulent kinetic energy near the free surface, discussed in the previous section, leads to overpredicted values of ν_t near the free surface, which could help explain the difference in air concentration near the pseudo-bottom as well as in the step cavities. Z_{90} also shows great agreement with the experimental data. In addition, the Z_{90} profile indicates how as more bubbles are incorporated into the flow, the free surface rises. Overall, the model shows a very promising capability to simulate self-aerated flows.

6. Discussion and conclusions

A new methodology for the simulation of self-aerated flows under a RANS framework was presented. The new method was validated for four scenarios of different complexity, showing satisfactory results for all of them. The proposed methodology presents several advantages compared to existing models:

- The governing equations are derived rigorously from the multi-fluid equations, providing what we perceive as a better representation of the physics of the flow. There are no strong assumptions limiting the analysis.
- The air-entrainment does not depend on a function that defines how much air is incorporated into the flow, but on a local balance between bubble diffusivity and rising velocity that does not require calibration and has shown to provide much better agreement with the experimental data.
- The coupling of the air-entrainment model with the free surface resolution algorithm provides a consistent modification of the free surface elevation with the amount of bubbles incorporated into or eliminated from the flow.
- The coupling between the four governing equations (α_m Eq. (11), α_b Eq. (13), momentum Eq. (22) and pressure Eq. (57)) allows representing important phenomena in highly aerated flows such as the modification of the flow features and the alteration of the free surface shape due to the presence of the dispersed phase.
- The approach is general, as it is intended not only for open-channel flows but also for jets and dropshafts.

Some limitations arise from the application of a RANS framework. The process of self-aeration is highly unsteady, with time scales filtered out after Reynolds averaging. This leads to a simplification of the physics that requires several closures that can affect the reliability of the model. Another limitation of this framework is the assumption of incompressibility of the bubbles. The volume occupied by the dispersed air is considered constant and does not take into account the changes in the surrounding pressure. This effect is not very important in relatively shallow flows, such as channels and spillways, but it may be important in other scenarios, such as bubble plumes in deep tanks.

Some aspects of this model were simplified in the current version of the model to allow for a more condensed description of the new methodology, but will be analyzed in future studies. Some of them are:

- Even though it is well known that bubbles have an effect on the modulation of turbulence, single-phase turbulent closures were used to represent the Reynolds stresses. Because the bubble diffusivity is considered proportional to the eddy viscosity, not considering the effect of the bubbles on the turbulence closure can impact in the amount of air entrained as well as its distribution. Turbulent closures have to be modified to account for the presence of bubbles and buoyancy effects.
- The regions where air entrainment occurs were defined manually based on the experimental results. They should be defined automatically by the model. Different criteria to evaluate the occurrence of air entrainment exist and will be evaluated on future work.
- The bubble diameter was defined manually. Ideally, this parameter should be a result of the model itself.
- The proportionality between bubble diffusivity and eddy viscosity is given by the Schmidt number. The definition of this parameter may vary for different flows and have to be studied in more detail and with appropriate turbulent closures.

Self-aerated flows are present in many engineering problems, and experimental and numerical techniques available for their study still present several limitations. We believe that this study provides significant advancement in the current capabilities of studying these flows with numerical methods, and can be used for the design and study flows on prototype scale.

Declaration of competing interest

The authors declare that they have no known competing financial interests or personal relationships that could have appeared to influence the work reported in this paper.

Data availability

Data will be made available on request.

Supplementary data

Supplementary material related to this article can be found online at https://doi.org/10.1016/j.cma.2023.115958.

References

[1] H.A. Domitrovic, J.A. Bechara, C. Flores Quintana, J.P. Roux, G. Gavilán, A survey study of gas supersaturation and fish gas bubble disease in the Paraná river below Yacyretá dam, Argentina, Rev. Ictiol. 8 (1/2) (2000) 29–40.
[2] H.T. Falvey, Air-Water Hydraulic Flow in Structures United of the Interior, Water and Power Resources Service Engineering and Research Center, Denver, 1980.
[3] I.R. Wood, Air entrainment in free-surface flows, in: IAHR Hydraulic Design Considerations, Routledge, 2018, http://dx.doi.org/10.1201/9781315137049.
[4] H.T. Falvey, Cavitation in Chutes and Spillways, no. 42, Bureau of Reclamation, Denver, 1990.
[5] H. Chanson, On air entrapment onset and surface velocity in high-speed turbulent prototype flows, Flow Meas. Instrum. 83 (2022) 102–122, http://dx.doi.org/10.1016/j.flowmeasinst.2022.102122.
[6] F. Zabaleta, F.A. Bombardelli, Eddy-resolving simulation of flows over macro-roughness, in: River Flow 2020 - Proceedings of the 10th Conference on Fluvial Hydraulics, 2020, pp. 1293–1299, http://dx.doi.org/10.1201/b22619-179.
[7] H. Chanson, Air Bubble Entrainment in Free-Surface Turbulent Shear Flows, Elsevier, 1996, http://dx.doi.org/10.1016/B978-0-12-168110-4.X5000-0.
[8] L.G. Straub, A.G. Anderson, Experiments on self-aerated flow in open channels, J. Hydraul. Div. 84 (7) (1958) 1–35, http://dx.doi.org/10.1061/JYCEAJ.0000261.

[9] L.G. Straub, A.G. Anderson, Self-aerated flow in open channels, Trans. Am. Soc. Civ. Eng. 125 (1) (1960) 456–481, http://dx.doi.org/10.1061/TACEAT.0007889.
[10] S. Felder, H. Chanson, Aeration, flow instabilities, and residual energy on pooled stepped spillways of embankment dams, J. Irrig. Drain. Eng. 139 (10) (2013) 880–887, http://dx.doi.org/10.1061/(ASCE)IR.1943-4774.0000627.
[11] J. Leandro, D.B. Bung, R. Carvalho, Measuring void fraction and velocity fields of a stepped spillway for skimming flow using non-intrusive methods, Exp. Fluids 55 (5) (2014) 1732, http://dx.doi.org/10.1007/s00348-014-1732-6.
[12] H. Chanson, T. Brattberg, Experimental study of the air-water shear flow in a hydraulic jump, Int. J. Multiph. Flow. 26 (4) (2000) 583–607, http://dx.doi.org/10.1016/S0301-9322(99)00016-6.
[13] F. Murzyn, D. Mouaze, J.R. Chaplin, Optical fibre probe measurements of bubbly flow in hydraulic jumps, Int. J. Multiph. Flow. 31 (1) (2005) 141–154, http://dx.doi.org/10.1016/j.ijmultiphaseflow.2004.09.004.
[14] H. Chanson, S. Aoki, A. Hoque, Physical modelling and similitude of air bubble entrainment at vertical circular plunging jets, Chem. Eng. Sci. 59 (4) (2004) 747–758, http://dx.doi.org/10.1016/j.ces.2003.11.016.
[15] S. Felder, Air-Water Flow Properties on Stepped Spillways for Embankment Dams: Aeration, Energy Dissipation and Turbulence on Uniform, Non-Uniform and Pooled Stepped Chutes (Ph.D. Thesis), School of Civil Engineering, Univ. of Queensland, Australia, 2013.
[16] M. Kramer, B. Hohermuth, D. Valero, S. Felder, Best practices for velocity estimations in highly aerated flows with dual-tip phase-detection probes, Int. J. Multiph. Flow. 126 (2020) 103228, http://dx.doi.org/10.1016/j.ijmultiphaseflow.2020.103228.
[17] P.M. Carrica, D. Drew, F. Bonetto, R.T. Lahey, A polydisperse model for bubbly two-phase flow around a surface ship, Int. J. Multiph. Flow. 25 (2) (1999) 257–305, http://dx.doi.org/10.1016/S0301-9322(98)00047-0.
[18] D.T. Souders, C.W. Hirt, Modeling entrainment of air at turbulent free surfaces, in: Critical Transitions in Water and Environmental Resources Management, no. 505, American Society of Civil Engineers, Reston, VA, 2004, pp. 1–10, http://dx.doi.org/10.1061/40737(2004)187.
[19] A. Gonzales, F.A. Bombardelli, Two-phase-flow theoretical and numerical models for hydraulic jumps, including air entrainment, in: Proceedings of the 31st IAHR World Congress, Seoul 2005, 2005.
[20] J. Ma, A.A. Oberai, D.A. Drew, J. Richard T. Lahey, M.C. Hyman, A comprehensive sub-grid air entrainment model for rans modeling of free-surface bubbly flows, J. Comput. Multiph. Flows 3 (1) (2011) 41–56, http://dx.doi.org/10.1260/1757-482X.3.1.41.
[21] A.M. Castro, J. Li, P.M. Carrica, A mechanistic model of bubble entrainment in turbulent free surface flows, Int. J. Multiph. Flow. (2016) http://dx.doi.org/10.1016/j.ijmultiphaseflow.2016.07.005.
[22] P. Lopes, G. Tabor, R.F. Carvalho, J. Leandro, Explicit calculation of natural aeration using a Volume-of-Fluid model, Appl. Math. Model. 40 (17–18) (2016) 7504–7515, http://dx.doi.org/10.1016/j.apm.2016.03.033.
[23] P. Lopes, J. Leandro, R.F. Carvalho, D.B. Bung, Alternating skimming flow over a stepped spillway, Environ. Fluid Mech. 17 (2) (2017) 303–322, http://dx.doi.org/10.1007/s10652-016-9484-x.
[24] C.J. Greenshields, OpenFOAM User Guide v7, CFD Direct Ltd., 2019.
[25] Z. Dong, J. Wang, D.F. Vetsch, R.M. Boes, G. Tan, Numerical simulation of air-water two-phase flow on stepped spillways behind X-shaped flaring gate piers under very high unit discharge, Water 11 (10) (2019) http://dx.doi.org/10.3390/w11101956.
[26] B. Hohermuth, L. Schmocker, R.M. Boes, D.F. Vetsch, Numerical simulation of air entrainment in uniform chute flow, J. Hydraul. Res. (2020) http://dx.doi.org/10.1080/00221686.2020.1780492.
[27] S.K. Almeland, T. Mukha, R.E. Bensow, An improved air entrainment model for stepped spillways, Appl. Math. Model. 100 (2021) 170–191, http://dx.doi.org/10.1016/j.apm.2021.07.016.
[28] P. Lopes, J. Leandro, R.F. Carvalho, Self-aeration modelling using a sub-grid Volume-Of-Fluid model, Int. J. Nonlinear Sci. Numer. Simul. 18 (7–8) (2017) 559–574, http://dx.doi.org/10.1515/ijnsns-2017-0015.
[29] L. Deike, W.K. Melville, S. Popinet, Air entrainment and bubble statistics in breaking waves, J. Fluid Mech. 801 (2016) 91–129, http://dx.doi.org/10.1017/jfm.2016.372.
[30] M. Mortazavi, V. Le Chenadec, P. Moin, A. Mani, Direct numerical simulation of a turbulent hydraulic jump: Turbulence statistics and air entrainment, J. Fluid Mech. 797 (2016) 60–94, http://dx.doi.org/10.1017/jfm.2016.230.
[31] X. Yu, K. Hendrickson, D.K.P. Yue, Scale separation and dependence of entrainment bubble-size distribution in free-surface turbulence, J. Fluid Mech. 885 (2019) 1–12, http://dx.doi.org/10.1017/jfm.2019.986.
[32] W.H.R. Chan, P.L. Johnson, P. Moin, J. Urzay, The turbulent bubble break-up cascade. Part 2. Numerical simulations of breaking waves, J. Fluid Mech. 912 (2021) 1–39, http://dx.doi.org/10.1017/jfm.2020.1084.
[33] A. Witt, J. Gulliver, L. Shen, Simulating air entrainment and vortex dynamics in a hydraulic jump, Int. J. Multiph. Flow. 72 (2015) http://dx.doi.org/10.1016/j.ijmultiphaseflow.2015.02.012.
[34] V. Jesudhas, R. Balachandar, H. Wang, F. Murzyn, Modelling hydraulic jumps: IDDES versus experiments, Environ. Fluid Mech. 20 (2) (2020) 393–413, http://dx.doi.org/10.1007/s10652-019-09734-5.
[35] G.G. Pereira, M. Dufresne, J. Wertel, J. Vazquez, Simulation of self-aerated flows by switching interface closures, J. Hydraul. Res. 59 (5) (2021) 766–778, http://dx.doi.org/10.1080/00221686.2020.1844809.
[36] S.D. Márquez, N.M. Nigro, An extended mixture model for the simultaneous treatment of small-scale and large-scale interfaces, Internat. J. Numer. Methods Fluids 75 (8) (2014) 547–574, http://dx.doi.org/10.1002/fld.3906.
[37] O.Y. Shonibare, K.E. Wardle, Numerical investigation of vertical plunging jet using a hybrid multifluid-VOF multiphase CFD solver, Int. J. Chem. Eng. 2015 (2015) http://dx.doi.org/10.1155/2015/925639.
[38] S. Felder, H. Chanson, Air-water flow characteristics in high-velocity free-surface flows with 50% void fraction, Int. J. Multiph. Flow. 85 (2016) 186–195, http://dx.doi.org/10.1016/j.ijmultiphaseflow.2016.06.004.
[39] B.S. Mirjalili, S.S. Jain, M.S. Dodd, Interface-capturing methods for two-phase flows: An overview and recent developments, Cent. Turbul. Res. Annu. Res. Briefs 1 (2017) 117–135.

[40] D.A. Drew, S.L. Passman, Theory of Multicomponent Fluids, Springer-Verlag, New York, 2014.
[41] S.C. Wilhelms, J.S. Gulliver, Bubbles and waves description of self-aerated spillway flow, J. Hydraul. Res. 43 (5) (2005) 522–531, http://dx.doi.org/10.1080/00221680509500150.
[42] D. Valero, D.B. Bung, Reformulating self-aeration in hydraulic structures: Turbulent growth of free surface perturbations leading to air entrainment, Int. J. Multiph. Flow. 100 (2018) 127–142, http://dx.doi.org/10.1016/j.ijmultiphaseflow.2017.12.011.
[43] D.Z. Zhang, A. Prosperetti, Averaged equations for inviscid disperse two-phase flow, J. Fluid Mech. 267 (1994) 185–219, http://dx.doi.org/10.1017/S0022112094001151.
[44] P. Bohorquez, Finite volume method for falling liquid films carrying monodisperse spheres in Newtonian regime, AIChE J. 58 (8) (2012) 2601–2616, http://dx.doi.org/10.1002/aic.13863.
[45] M. Ouda, E.A. Toorman, Development of a new multiphase sediment transport model for free surface flows, Int. J. Multiph. Flow. 117 (2019) 81–102, http://dx.doi.org/10.1016/j.ijmultiphaseflow.2019.04.023.
[46] D.A. Drew, Mathematical modeling of two-phase flow, Annu. Rev. Fluid Mech. 15 (1) (1983) 261–291, http://dx.doi.org/10.1146/annurev.fl.15.010183.001401.
[47] E. Berberovic, N.P. van Hinsberg, S. Jakirlic, I.V. Roisman, C. Tropea, Drop impact onto a liquid layer of finite thickness: Dynamics of the cavity evolution, Phys. Rev. E 79 (2009) 036306, http://dx.doi.org/10.1103/PhysRevE.79.036306.
[48] M. Manninen, V. Taivassalo, On the mixture model for multiphase flow, VTT Publ. 288 (1996) 3–67.
[49] M. Ishii, T. Hibiki, Thermo-Fluid Dynamics of Two-Phase Flow, no.4, Springer, New York, NY, 2011, pp. 1–23, http://dx.doi.org/10.1007/978-1-4419-7985-8.
[50] J.R. Grace, Shapes and velocities of bubbles rising in infinite liquids, Trans. Inst. Chem. Eng. 51 (1973) 116–120.
[51] A. Wüest, N.H. Brooks, D.M. Imboden, Bubble plume modeling for lake restoration, Water Resour. Res. 28 (12) (1992) 3235–3250, http://dx.doi.org/10.1029/92WR01681.
[52] S.S. Deshpande, L. Anumolu, M.F. Trujillo, Evaluating the performance of the two-phase flow solver interFoam, Comput. Sci. Discov. 5 (1) (2012) 014016, http://dx.doi.org/10.1088/1749-4699/5/1/014016.
[53] I.C. Meireles, F.A. Bombardelli, J. Matos, Air entrainment onset in skimming flows on steep stepped spillways: An analysis, J. Hydraul. Res. 52 (3) (2014) 375–385, http://dx.doi.org/10.1080/00221686.2013.878401.
[54] S. Márquez Damián, J.M. Giménez, N.M. Nigro, gdbOF: A debugging tool for OpenFOAM®, Adv. Eng. Softw. 47 (1) (2012) 17–23, http://dx.doi.org/10.1016/j.advengsoft.2011.12.006.
[55] T. Holzmann, Mathematics, Numerics, Derivations and OpenFOAM®, 2019.
[56] F. Moukalled, L. Mangani, M. Darwish, The finite volume method in computational fluid dynamics: an advanced introduction with openfoam and matlab, in: Fluid Mechanics and Its Applications, Springer International Publishing, 2015.
[57] S.T. Zalesak, Fully multidimensional flux-corrected transport algorithms for fluids, J. Comput. Phys. 31 (1979) 335–362.
[58] S. Márquez Damián, An Extended Mixture Model for the Simultaneous Treatment of Small-Scale and Large-Scale Interfaces (Ph.D. Thesis), Universidad Nacional del Litorial, 2013.
[59] C. Hirsch, Numerical Computation of Internal and External Flows, second ed., Butterworth-Heinemann, Oxford, 2007, pp. 1–V, http://dx.doi.org/10.1016/B978-075066594-0/50039-4.
[60] U.M. Ascher, S.J. Ruuth, B.T.R. Wetton, Implicit-explicit methods for time-dependent partial differential equations, SIAM J. Numer. Anal. 32 (3) (1995) 797–823, http://dx.doi.org/10.1137/0732037.
[61] M.J. Friedl, T.K. Fanneløp, Bubble plumes and their interaction with the water surface, Appl. Ocean Res. 22 (2) (2000) 119–128, http://dx.doi.org/10.1016/S0141-1187(99)00022-X.
[62] A. Amador, Comportamiento Hidráulico de Los Aliviaderos Escalonados En Presas De Hormigón Compactado (Ph.D. Thesis), Polytechnic Univ. of Catalonia (UPC), Barcelona, Spain, 2005, (in Spanish).
[63] H.G. Weller, A New Approach to VOF-Based Interface Capturing Methods for Incompressible and Compressible Flow, Technical Report, May, OpenCFD, 2008.
[64] F.A. Bombardelli, Turbulence in Multiphase Models for Aeration Bubble Plumes (Ph.D. Thesis), University of Illinois, Urbana-Champaign, 2004.
[65] D.P. Hamilton, S.G. Schladow, Prediction of water quality in lakes and reservoirs. Part I — Model description, Ecol. Model. 96 (1) (1997) 91–110, http://dx.doi.org/10.1016/S0304-3800(96)00062-2.
[66] T.K. Fanneløp, K. Sjoen, Hydrodynamics of underwater blowouts, in: 18th Aerospace Sciences Meeting, 2000, http://dx.doi.org/10.2514/6.1980-219.
[67] C. Sasmal, Unsteady motion past a sphere translating steadily in wormlike micellar solutions: A numerical analysis, J. Fluid Mech. 912 (2021) A52, http://dx.doi.org/10.1017/jfm.2020.1164.
[68] C. Gualtieri, A. Angeloudis, F. Bombardelli, S. Jha, T. Stoesser, On the values for the turbulent Schmidt number in environmental flows, Fluids 2 (2) (2017) http://dx.doi.org/10.3390/fluids2020017.
[69] B. Devolder, P. Rauwoens, P. Troch, Application of a buoyancy-modified k-ω SST turbulence model to simulate wave run-up around a monopile subjected to regular waves using OpenFOAM®, Coast. Eng. 125 (June 2016) (2017) 81–94, http://dx.doi.org/10.1016/j.coastaleng.2017.04.004.
[70] B.E. Larsen, D.R. Fuhrman, On the over-production of turbulence beneath surface waves in Reynolds-averaged Navier-Stokes models, J. Fluid Mech. 853 (2018) 419–460, http://dx.doi.org/10.1017/jfm.2018.577.
[71] N. Rajaratnam, Skimming flow in stepped spillways, J. Hydraul. Eng. 116 (4) (1990) 587–591, http://dx.doi.org/10.1061/(ASCE)0733-9429(1990)116:4(587).
[72] G. Halbronn, Étude de la mise en régime des écoulements sur les ouvrages á forte pente: Application au probléme de l'entrainement d'air. (Analysis of flows on hydraulic structures with a large slope: Application to air entrainment problem), Houille Blanche (1952).

[73] G. Halbronn, Discussion to turbulent boundary layer on steep slopes, Transp. Eng. J. ASCE 119 (1954) 1234–1240.
[74] W.J. Bauer, Turbulent boundary layer on steep slopes, Transp. Eng. J. ASCE 119 (1954) 1212–1233.
[75] J.P. Toro, F.A. Bombardelli, J. Paik, Detached eddy simulation of the nonaerated skimming flow over a stepped spillway, J. Hydraul. Eng. 143 (9) (2017) 04017032, http://dx.doi.org/10.1061/(ASCE)HY.1943-7900.0001322.
[76] F. Zabaleta, F.A. Bombardelli, J.P. Toro, Towards an understanding of the mechanisms leading to air entrainment in the skimming flow over stepped spillways, Environ. Fluid Mech. (2020) http://dx.doi.org/10.1007/s10652-019-09729-2.
[77] F.A. Bombardelli, I. Meireles, J. Matos, Laboratory measurements and multi-block numerical simulations of the mean flow and turbulence in the non-aerated skimming flow region of steep stepped spillways, Environ. Fluid Mech. 11 (3) (2011) 263–288.
[78] I. Meireles, F. Renna, J. Matos, F. Bombardelli, Skimming, nonaerated flow on stepped spillways over roller compacted concrete dams, J. Hydraul. Eng. 138 (10) (2012) 870–877, http://dx.doi.org/10.1061/(ASCE)HY.1943-7900.0000591.
[79] J.P. Toro, F.A. Bombardelli, J. Paik, I. Meireles, A. Amador, Characterization of turbulence statistics on the non-aerated skimming flow over stepped spillways: A numerical study, Environ. Fluid Mech. 16 (6) (2016) 1195–1221, http://dx.doi.org/10.1007/s10652-016-9472-1.